Author's personal copy

Advances in Colloid and Interface Science 165 (2011) 70–90

Contents lists available at ScienceDirect

Advances in Colloid and Interface Science

journal homepage: www.elsevier.com/locate/cis

Theory of non-equilibrium force measurements involving deformable drops and bubbles

Derek Y.C. Chan [a,b,c,*], Evert Klaseboer [b], Rogerio Manica [b]

[a] Particulate Fluids Processing Centre, Department of Mathematics and Statistics, University of Melbourne, Parkville, 3010, Australia
[b] Institute of High Performance Computing, 1 Fusionopolis Way, 138632, Singapore
[c] Department of Mathematics, National University of Singapore, 117543, Singapore

ARTICLE INFO

Available online 24 December 2010

Keywords:
Young–Laplace
Stokes–Reynolds
Coalescence
Film drainage
AFM force measurements
Deformable drops and bubbles

ABSTRACT

Over the past decade, direct force measurements using the Atomic Force Microscope (AFM) have been extended to study non-equilibrium interactions. Perhaps the more scientifically interesting and technically challenging of such studies involved deformable drops and bubbles in relative motion. The scientific interest stems from the rich complexity that arises from the combination of separation dependent surface forces such as Van der Waals, electrical double layer and steric interactions with velocity dependent forces from hydrodynamic interactions. Moreover the effects of these forces also depend on the deformations of the surfaces of the drops and bubbles that alter local conditions on the nanometer scale, with deformations that can extend over micrometers. Because of incompressibility, effects of such deformations are strongly influenced by small changes of the sizes of the drops and bubbles that may be in the millimeter range. Our focus is on interactions between emulsion drops and bubbles at around 100 μm size range. At the typical velocities in dynamic force measurements with the AFM which span the range of Brownian velocities of such emulsions, the ratio of hydrodynamic force to surface tension force, as characterized by the capillary number, is ~10^{-6} or smaller, which poses challenges to modeling using direct numerical simulations. However, the qualitative and quantitative features of the dynamic forces between interacting drops and bubbles are sensitive to the detailed space and time-dependent deformations. It is this dynamic coupling between forces and deformations that requires a detailed quantitative theoretical framework to help interpret experimental measurements. Theories that do not treat forces and deformations in a consistent way simply will not have much predictive power. The technical challenges of undertaking force measurements are substantial. These range from generating drop and bubble of the appropriate size range to controlling the physicochemical environment to finding the optimal and quantifiable way to place and secure the drops and bubbles in the AFM to make reproducible measurements. It is perhaps no surprise that it is only recently that direct measurements of non-equilibrium forces between two drops or two bubbles colliding in a controlled manner have been possible. This review covers the development of a consistent theory to describe non-equilibrium force measurements involving deformable drops and bubbles. Predictions of this model are also tested on dynamic film drainage experiments involving deformable drops and bubbles that use very different techniques to the AFM to demonstrate that it is capable of providing accurate quantitative predictions of both dynamic forces and dynamic deformations. In the low capillary number regime of interest, we observe that the dynamic behavior of all experimental results reviewed here are consistent with the tangentially immobile hydrodynamic boundary condition at liquid–liquid or liquid–gas interfaces. The most likely explanation for this observation is the presence of trace amounts of surface-active species that are responsible for arresting interfacial flow.

Crown Copyright © 2010 Published by Elsevier B.V. All rights reserved.

Contents

* Corresponding author. Particulate Fluids Processing Centre, Department of Mathematics and Statistics, University of Melbourne, Parkville, 3010, Australia. Tel.: +61 1 8344 5556; fax: +61 3 8344 4599.
E-mail address: D.Chan@unimelb.edu.au (D.Y.C. Chan).

0001-8686/$ – see front matter. Crown Copyright © 2010 Published by Elsevier B.V. All rights reserved.
doi:10.1016/j.cis.2010.12.001

Author's personal copy

1. Introduction

1.1. Background and motivations

Studies of non-equilibrium interactions involving deformable drops and bubbles predated the formulation of the Derjaguin–Landau–Verwey–Overbeek theory of colloidal stability [1,2] with the studies of Derjaguin and Kussakov [3] on time-dependent behavior of a rising bubble towards a flat plate under buoyancy force. Subsequent non-equilibrium studies concentrated on the drainage phenomena of the liquid film between deformable menisci [4].

Early direct measurements of non-equilibrium forces were based on the Surface Forces Apparatus to measure the time-dependent approach between two cross-cylinders of mica down to nanometer separations in aqueous [5] and non-aqueous liquids [6]. Forces under conditions of steady state oscillations of the mica surfaces were also studied in the context of examining the possible variations in fluid viscosities of nanometer thick confined liquid films [7] and the lubricating properties of adsorbed polymers [8].

With the advent of the atomic force microscope, interest continued in the hydrodynamic interaction involving solid spheres in the tens of micrometer size range. Although much interest was generated by reports of hydrodynamic boundary slip at the solid–liquid interface [9], particularly in the context of microfluidic applications [10], recent repeated measurements suggest that instrumental artifacts are likely to be responsible for such observations at smooth well defined surfaces [11–13].

In the first applications of the atomic force microscope to measure equilibrium forces involving deformable bubbles, the deformational response of the bubble was treated as a Hookean spring [14,15]. In subsequent equilibrium studies involving drops, the Young–Laplace equation was used to account for the drop deformational behavior [16,17].

In considering non-equilibrium interactions, the time-dependent force between, for instance, two approaching deformable drops at any instant, does not only depend on the instantaneous shapes and separation between the drops, but also on initial conditions that determine the drop shape and interfacial velocities. In addition, flow of the continuous fluid phase also contributes to the hydrodynamic interaction. Therefore appropriate experimental data needs to be recorded to provide initial and boundary conditions for theoretical analysis.

Author's personal copy

Another challenge in dealing with deformable bodies is the issue of having multiple length scales of very different magnitudes. For non-deforming bodies, only the geometry around the interaction zone between surfaces in close proximity needs to be specified in order to determine the interaction force, using say, the Derjaguin approximation [18,19]. For deformable bodies, on the other hand, a mechanical equation of state connects local variations of the interaction force and the local geometry [20]. If the deformable material is incompressible, this coupling between forces and geometries can extend over length scales of many orders of magnitude. For example, the interaction between millimeter size drops or bubbles across films of nanometer thickness can cause deformations extending over tens to hundreds of micrometers. Furthermore, the incompressibility of drops and to a good approximation, bubbles, means that small changes on the scale of the size of drops or bubbles can have significant effects on the scale of thin films. As a consequence, approaches based on direct numerical simulations are unlikely to have sufficient resolution and precision to span such a large range of length scales.

The intuition we obtain in studying drops and bubbles where their deformational response to applied forces can be well characterized is also valuable in analyzing interactions involving other types of soft deformable bodies that may have elastic or viscoelastic responses.

1.2. Perspective and scope

There are three key elements that must be included in modeling time-dependent interactions involving deformable drops and bubbles:

(a) A description of how drops/bubbles deform under the influence of stresses arising from hydrodynamic flow and disjoining pressure from surface forces,
(b) A description of the flow of the intervening fluid within the thin film confined by the deformable surfaces of drops or bubbles, and
(c) A consideration of surface or colloidal forces that will vary with local deformations of the interfaces in close proximity.

All such factors determine collision stability or coalescence and must of course be treated in a self-consistent way. For instance, the deformed interfaces of the drops or bubbles determine the boundaries of the thin film where the intervening fluid must flow during interaction. However, such flow will generate pressure profiles within the film that will in turn determine the shape of the interfaces. For instance, the application of the Stefan–Reynolds Flat Film Model [21,22] to model film drainage in which the drop interfaces are assumed to be plane parallel, immediately gives rise to internal inconsistencies that require subsequent correction. Indeed the use of this model, in spite of its inability to give quantitative agreement with even the simplest experiments, has in our view distorted our understanding of non-equilibrium interactions between deformable drops and bubbles.

At the typical velocities in dynamic force measurement with the AFM which also span the range of Brownian velocities of such emulsions (~100 μm size) or at velocities used to study dynamic film drainage in mm size drops and bubbles the ratio of hydrodynamic force to surface tension force, as characterized by the capillary number, $Ca \equiv \mu V/\sigma$ is $\sim 10^{-6}$ or smaller. Here μ is the viscosity of the continuous phase, V a characteristic velocity and σ the interfacial tension.

Under such conditions the theory in this review treats hydrodynamic interactions in the low Reynolds number or Stokes flow regime relevant to many measurements of non-equilibrium forces using the atomic force microscope as well as direct observations of time-dependent deformations of drops and bubbles that are undergoing interactions. Flow in the thin film trapped by the deforming drops (or bubbles) is considered in the lubrication approximation because the film thickness is small compared to the lateral dimension of the film. Deformations of the interfaces of the drops or bubbles are determined by the combination of capillary forces, hydrodynamic and disjoining pressure. Spatial and temporal evolution of the deformations of the interfaces of the drops or bubbles as a result of interaction are modeled in detail whereas deformations of the rest of the drops or bubbles are treated analytically to provide boundary conditions that reflect how the interacting drops or bubbles are driven together.

An alternate approach to treat hydrodynamic interactions is to solve the complete Stokes flow equations using direct numerical simulations [23–26]. Such methods have been used to study drop coalescence for capillary numbers in the range: Ca ~0.001–0.1, where the computational time for a collision encounter can take over 100 h of CPU time. However, for capillary numbers of interest in film deformation and force measurement experiments considered here where $Ca \sim 10^{-6}$, a direct numerical approach has yet to be attempted. In contrast, the model we outline here takes advantage of the simplifications afforded by the special characteristics of film drainage and AFM force measurement experiments whereby we can undertake calculation of a typical drainage or force run in around 1 min on a notebook computer.

In order to focus on the key physical principles, we shall only consider non-equilibrium interaction between deformable drops and bubbles for which there is axial symmetry. As we shall see in Section 5, this is relevant to a number of different experiments that measure non-equilibrium forces and deformations of drops and bubbles.

The equations that govern the deformation of drops and bubbles will be developed in Section 2. In particular, details of how to obtain boundary conditions using the asymptotic analytic solutions for the drop shape outside the film will be given. Different models for hydrodynamic interactions, including the familiar Stefan–Reynolds Flat Film Model, will be discussed in Section 3. The Stokes–Reynolds–Young–Laplace model for describing non-equilibrium interactions between deformable drops and bubbles, incorporating the development in Sections 2 and 3 will be studied using perturbation analysis in Section 4 and detailed implementation of robust numerical solutions of the equations will also be given. In Section 5, predictions of the Stokes–Reynolds–Young–Laplace model are compared with experiments that measure dynamic deformations and dynamic forces to illustrate the utility of the model.

This review is therefore aimed at readers who are familiar with established theories of surface forces and disjoining pressures at the level of the Derjaguin–Landau–Verwey–Overbeek (DLVO) model. In addition, the reader should have some familiarity with the basic operations and limitations of the atomic force microscope when it is used to measure forces between rigid surfaces.

2. Drop and bubble deformations

In this section, we develop the equations that govern the deformation of a drop or bubble as a result of external forces arising from the interaction with another particle or drop. Since in most cases, the behavior of drops and bubbles is very similar, we will henceforth use the term “drops” to denote both drops and bubbles unless specified otherwise explicitly.

About 200 years ago in 1805, the British physician Thomas Young [27] gave an analysis of the shape of a deformable fluid interface under the action of capillary forces without using any equations. The French astronomer Pierre-Simon Laplace [28] considered the same problem using a force balance method in the normal and tangential direction to the fluid interface. Carl Friedrich Gauss [29] gave an analysis of the problem in terms of the principle of minimization of interfacial area under the action of interfacial tension or energy. Strictly speaking such an approach is not applicable under non-equilibrium conditions. In the presence of hydrodynamic interaction that is of interest here, we can estimate the time scale required for a

Author's personal copy

drop, under capillary forces, to adjust its shape in response to external perturbations. Capillary waves of velocity c and wavelength λ on a spherical drop with interfacial tension σ_o obey the dispersion relation [30]: $c^2 = 2\pi\sigma_o/[\lambda\ (\rho_d + \rho_e)]$, with ρ_d and ρ_e being the densities of the dispersed and continuous phases. Taking $\lambda \sim 100\ \mu m$ which is an upper limit of the size of the deformation zone of small drops, gives $c \sim 1$ m/s, which is much faster than the characteristic approach velocities of drops considered here. In other words, in the presence of hydrodynamic interactions, we make the reasonable assumption that a drop can adjust its shape instantaneously to accommodate changes in the hydrodynamic pressure. Thus we can add the effects of the hydrodynamic pressure, p to effects due to equilibrium disjoining pressure arising from surface forces.

2.1. Augmented Young–Laplace equation

Consider a sessile drop on a substrate, immersed in a continuous medium as shown in Fig. 1. It is deformed by interactions due to surface forces between itself and a solid particle located at a distance D from the substrate. If the range of the surface forces is small compared to the dimensions of the drop and the particle, the deformation will be confined to a small interaction zone of radius a around the apex of the drop. Within the Derjaguin approximation the drop–particle interaction is given in terms of an interaction free energy per unit area, $E(h)$ or the disjoining pressure $\Pi(h) \equiv -\mathrm{d}E(h)/\mathrm{d}h$. These quantities are assumed to be known functions of the film thickness $h(r,t)$ around the axisymmetric drop which may change slowly with time, t. We assume the drop has constant interfacial tension or surface energy per unit area, σ_o.

The equilibrium deformation of a drop can be obtained by minimizing the Helmholtz surface energy of the system that can be written in terms of the drop height $z(r,t)$ [29]. This method has been used to derive the equation for an equilibrium drop under external forces [31–35]. The surface energy minimization also gives the Young–Dupré condition: $\sigma_o \cos\theta + \sigma_L = \sigma_S$ for the equilibrium contact angle θ at the base of the drop that is far from the interaction zone at the apex of the drop (see Fig. 1).

However, to describe dynamic deformations for which the principle of energy minimization would not strictly apply, we can adopt a quasi-static force balance approach that is a generalization of the method due to Laplace.

Consider an area element of the interface of an axisymmetric drop (Fig. 1) where surface tension forces act on the perimeter of the element along the interface and the pressure difference across the interface acts in the direction of the surface normal. In the polar direction, the surface tension forces along a longitude on two opposing sides of the area element of length $r(\varphi)\ d\alpha$ and $r(\varphi + d\varphi)\ d\alpha$ are:

$$\mathbf{F}^{\sigma}_{polar} = -\sigma_o[r(\varphi)d\alpha]\mathbf{t}(\varphi) + \sigma_o[r(\varphi + d\varphi)d\alpha]\mathbf{t}(\varphi + d\varphi) \tag{2.1.1}$$

where σ_o is the interfacial tension, $\mathbf{n}$ and $\mathbf{t}$ are the outward unit normal vector and unit tangent vector respectively, and the angles α and φ are defined in Fig. 1. Using the explicit expressions for these unit vectors: $\mathbf{n} = sin\varphi\,\hat{r} + cos\varphi\,\hat{z}$ and $\mathbf{t} = cos\varphi\,\hat{r} - sin\varphi\,\hat{z}$, we expand Eq. (2.1.1) to first order in $d\alpha$ and $d\varphi$ to give

$$\mathbf{F}^{\sigma}_{polar} = \sigma_o \frac{dr}{d\varphi} d\varphi\, d\alpha \quad \mathbf{t} - \sigma_o\, r\, d\varphi\, d\alpha\ \mathbf{n} \tag{2.1.2}$$

Similarly, in the azimuthal direction, we have the unit vectors: $\hat{\alpha} = -sin\alpha\,\hat{x} + cos\alpha\,\hat{y}$, $\hat{r} = cos\alpha\,\hat{x} + sin\alpha\,\hat{y} = sin\varphi\,\mathbf{n} + cos\varphi\,\mathbf{t}$, with $d\hat{\alpha}/d\alpha = -\hat{r}$, (Fig. 1) so the surface tension forces along a latitude on two opposing sides of the area element of length ds are to linear order in the change in azimuthal angle $d\alpha$:

$$\begin{aligned} \mathbf{F}^{\sigma}_{azimuth} &= \{-\sigma_o\hat{\alpha} + \sigma_o\hat{\alpha}(\alpha + d\alpha)\}ds \\ &= -\sigma_o\,\hat{r}\,d\alpha\,ds \\ &= -\sigma_o\ sin\varphi\ d\alpha\,ds\ \mathbf{n} - \sigma_o\ cos\varphi\,d\alpha\,ds\ \mathbf{t} \end{aligned} \tag{2.1.3}$$

The normal force due to the pressure difference across the interface is:

$$\mathbf{F}_{normal} = \{p_{in} - (p_{out} + p + \Pi)\}ds\, r\, d\alpha\, \mathbf{n} \tag{2.1.4}$$

where p_{in} is the internal pressure of the drop, p_{out} is the ambient pressure outside the drop, p is the hydrodynamic pressure and Π is the disjoining pressure. The sign convention is that p and Π are positive if they act in the direction opposite to the outward surface unit normal vector, $\mathbf{n}$.

We obtain the augmented Young–Laplace equation by equating the normal components of the forces in Eqs. (2.1.2)–(2.1.4), and using $d\varphi/ds = (dr/ds)(d\varphi/dr) = \cos\varphi\ (d\varphi/dr)$

$$p_{in} - (p_{out} + p + \Pi) = \sigma_o\left(\frac{d\varphi}{ds} + \frac{sin\,\varphi}{r}\right) \tag{2.1.5a}$$

$$\frac{2\sigma_o}{R_L} - (p + \Pi) = \sigma_o\left(cos\,\varphi\,\frac{d\varphi}{dr} + \frac{sin\,\varphi}{r}\right) \tag{2.1.5b}$$

$$= \frac{\sigma_o}{r}\frac{d}{dr}(r\,sin\,\varphi) \tag{2.1.5c}$$

$$= -\frac{\sigma_o}{r}\frac{\partial}{\partial r}\left(\frac{r\,z_r}{(1 + z_r^2)^{1/2}}\right) \tag{2.1.5d}$$

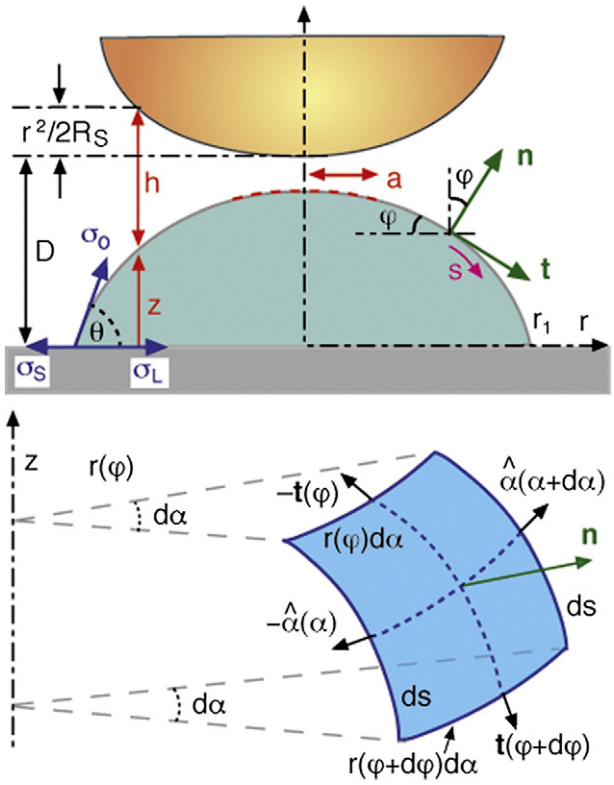

Fig. 1. Upper: Schematic of an axisymmetric sessile drop in a continuous phase, deformed around its apex within a small interaction zone of radius, a due to interaction with a solid particle with radius, R_s. Lower: An illustration of forces acting on a surface element of the axisymmetric sessile drop along the polar and azimuthal directions.

Author's personal copy

where $z_r \equiv \partial z/\partial r \equiv -\tan\varphi$, see Fig. 1. For later analysis, it is convenient to define the Laplace radius, R_L by

$$p_{in} - p_{out} \equiv \frac{2\sigma_o}{R_L} \tag{2.1.6}$$

Equating the tangential components of Eqs. (2.1.2) and (2.1.3) simply gives the identity $dr = \cos\varphi\, ds$ (see Fig. 1).

It is ironic that key equations in the theory of capillarity have been named after Thomas Young because in his writing, he managed to avoid the use of mathematical notations and equations altogether.

2.2. Special film shapes: Dimple, pimple, wimple and ripple

We can deduce a number of general results concerning drop deformation by taking the first integral of Eq. (2.1.5c) with respect to r to give

$$\sigma_o \; r\sin\varphi = \frac{\sigma_o r^2}{R_L} - \frac{1}{2\pi}\Phi(r,t) \tag{2.2.1a}$$

$$\Phi(r,t) \equiv 2\pi \int_0^r [p(r',t) + \Pi(r',t)]r' \; dr' \tag{2.2.1b}$$

where the function $\Phi(r,t)$ is related to the total force, $F(t)$

$$F(t) = 2\pi \int_0^\infty [p(r',t) + \Pi(r',t)]r' \, dr' \equiv \Phi(\infty,t) \tag{2.2.2}$$

acting on the drop due to the hydrodynamic pressure, p, and the disjoining pressure, Π. For $r \gg a$, both p and Π are negligible and Eq. (2.2.1a) for the drop shape outside the interaction zone can be written as

$$r\sin\varphi = \frac{r^2}{R_L} - \frac{F(t)}{2\pi\sigma_o}, \text{for } r \gg a. \tag{2.2.3}$$

The above result does not depend on the exact values of p and Π in the interaction zone, $r < a$. Thus the drop shape outside the interaction zone only depends on the total force $F(t)$. A very similar result was obtained some two centuries ago in Cartesian form [36,37]. Eq. (2.2.3) provides the necessary boundary condition for the numerical problem of solving for time deformations of the film, down to nanometer thickness in drainage and dynamic force experiments (see Section 4.1). The term in brackets on the RHS of Eq. (2.1.5a) is the sum of the local curvatures at the surface. Using Eq. (2.2.3) we can identify these curvatures outside the interaction zone to be

$$K_1 \equiv \frac{d\varphi}{ds} = \frac{1}{R_L} + \frac{1}{r^2}\frac{F(t)}{2\pi\sigma_o} \tag{2.2.4a}$$

$$K_2 \equiv \frac{\sin\varphi}{r} = \frac{1}{R_L} - \frac{1}{r^2}\frac{F(t)}{2\pi\sigma_o} \tag{2.2.4b}$$

where the hydrodynamic pressure, p and the disjoining pressure, Π are both negligible. We note that the sum of the curvatures $(K_1 + K_2)$ is independent of the force as expected from Eq. (2.1.5a).

We can now understand the physical origin of various film shapes observed and discussed in the literature. These shapes: the *pimple* [38], the *dimple* [39], the *wimple* [40] and the *ripple* [41] simply reflect the number of times the slope of the drop surface: $\partial z/\partial r \equiv -\tan\varphi$, becomes zero or changes sign. From Eq. (2.2.1a) we see that the sign of the slope is controlled by the quantity: $[(2\pi\sigma_o r^2/R_L) - \Phi(r,t)] \propto \sin\varphi \propto \partial z/\partial r$, that is only determined by the behavior of the Young–Laplace equation. This is the reason why dimple formation, for instance, appears in theories that have very different models for film drainage and surface mobility conditions [42–48].

2.3. Equation for thin film deformations

In this section we develop the governing equations for the thickness of the film between a deformable drop and a spherical particle and between two deformable drops in terms of the Young–Laplace equation of the previous section. In AFM force measurement experiments, drop deformation is localized in an interaction zone around the apex of the drop. Both the size of this zone and the extent of the deformation are small compared to the drop radius. This allows us to focus on the properties of the thin film. How this film is related to the rest of the drop outside the interaction zone will be considered in Section 2.4.

2.3.1. Film between a drop and a spherical particle

As drop deformations are confined to a small interaction zone within the radius $r \sim a$ around the apex, we seek a description of the shape of the film with thickness, $h(r,t)$ in this region. This film thickness is required to calculate the disjoining pressure, $\Pi(h)$ and to specify the film boundary in which hydrodynamic flow takes place. The geometric relation between $h(r,t)$ and the drop shape $z(r,t)$ follows from Fig. 1:

$$z(r,t) = D(t) + r^2/(2R_s) - h(r,t). \tag{2.3.1}$$

In the absence of a strong attraction between the drop and the particle, and certainly when the interaction is repulsive, we can expect the variation in the drop shape would be small on the scale of the drop size, that is, $z_r \equiv \partial z/\partial r \ll 1$ within the interaction zone. In this case, we only need to retain the linear term in z_r in Eq. (2.1.5d). On combining Eq. (2.3.1) with the linearized form of Eq. (2.1.5d) we have the following result for the equation of the film thickness, $h(r,t)$ between a drop and a spherical particle of radius, R_s that is valid in the interaction zone within the radius $r \sim a$

$$\frac{\sigma_o}{r}\frac{\partial}{\partial r}\left(r\frac{\partial h}{\partial r}\right) = \frac{2\sigma_o}{R_{ds}} - \Pi - p, \; 0 < r \sim a \;\; Drop-sphere \tag{2.3.2a}$$

$$\frac{1}{R_{ds}} \equiv \frac{1}{R_L} + \frac{1}{R_s} \tag{2.3.2b}$$

In the presence of a strong attraction between the drop and the particle, the drop shape, $z(r,t)$ may exhibit a cusp with an associated large gradient. However, in dynamic interactions involving deformable drops, this situation only occurs during the short time interval just prior to the last stage of a coalescence event. Therefore as we shall see in bubble–bubble coalescence experiments in Section 5.2.3, the fact that $\partial z/\partial r \ll 1$ may not be satisfied for the short time just prior to coalescence does not affect the ability of the theory to predict the form of the dynamic force leading up to coalescence and the actual coalescence time with good accuracy.

In general, Eq. (2.3.2a) has to be solved numerically when the disjoining pressure, Π and the hydrodynamic pressure, p are given. We stress that Eq. (2.3.2a) for the film thickness is obtained from a linearization of the augmented Young–Laplace equation, Eq. (2.1.3) and the geometric condition Eq. (2.3.1). Although the first term on the right hand side of Eq. (2.3.2a): $(2\sigma_o/R_{ds})$ has the dimensions of pressure, it is not the Laplace pressure of the drop. This is often a point of confusion in less than rigorous derivations of this result [49].

Author's personal copy

Eq. (2.3.2a) can be integrated twice to give

$$h(r,t) = h(0,t) + \frac{r^2}{2R_{ds}} - \frac{1}{2\pi\sigma_o}\, log\left(\frac{r}{2R_{dso}}\right)\Phi(r,t) + \frac{1}{2\pi\sigma_o}\,\Xi(r,t) \quad Drop-sphere \tag{2.3.3a}$$

$$\Xi(r,t) \equiv 2\pi \int_0^r [p(r',t) + \Pi(r',t)]r'\, log\left(\frac{r'}{2R_{dso}}\right)dr' \tag{2.3.3b}$$

where $h(0,t)$, the film thickness at $r=0$, is a constant of integration that is to be determined. The characteristic length scale of this drop–sphere problem is $R_{dso} \equiv (1/R_o + 1/R_s)^{-1}$, and it is used to scale the logarithmic terms in Eqs. (2.3.3a)–(2.3.3b). In the region $r>a$, the film thickness, h will become sufficiently large for Π and p to be negligible so that the value of r in the functions $\Phi(r,t)$ and $\Xi(r,t)$ may be replaced by infinity to yield the general outer asymptotic form of the film thickness

$$h(r,t) \to h(0,t) + \frac{r^2}{2R_{ds}} - \frac{F(t)}{2\pi\sigma_o}\, log\left(\frac{r}{2R_{dso}}\right) + H(R_{dso},t), r > a \quad Drop-sphere \tag{2.3.4}$$

$$H(R,t) \equiv \frac{1}{\sigma_o}\int_0^\infty [p(r',t) + \Pi(r',t)]r'\, log\left(\frac{r'}{2R}\right)\, dr' \tag{2.3.5}$$

Eq. (2.3.4) is the limiting form of the solution of the film shape Eq. (2.3.2a) between a drop with constant interfacial tension and a sphere. Although the constants $h(0,t)$ and $H(R_{dso},t)$ are as yet unknown at this stage, this solution can be matched to the solution valid outside the interaction zone (see Section 2.4) and provide us with the appropriate boundary conditions for the numerical solution of Eq. (2.3.2a). A result that is similar to Eq. (2.3.4) has been obtained by Yiantsios and Davis [23] who used a scaling analysis of the problem of two deformable drops approaching under a constant buoyancy force.

In Section 2.5, we will see that the logarithmic behavior for $r>a$ in Eq. (2.3.4) will match up with the inner asymptotic behavior of the outer solution of the augmented Young–Laplace equation Eq. (2.2.3) that will be developed in the next section. This result is analogous to Hooke's Law for a linear spring where the force exerted on the spring can be deduced from the extension. For a deformable drop, the total force, $F(t)$ acting on it is encoded in its geometric shape outside the interaction zone. This logarithmic limiting form of the film thickness has been observed experimentally [50].

Results for the special case of a drop interacting with a flat solid surface can be obtained from Eqs. (2.3.3a), (2.3.3b)–(2.3.5) in the limit of the sphere of infinite radius: $R_s \to \infty$.

2.3.2. Film between two drops

For two interacting drops denoted by $i=1$ or 2, with drop shape, $z_i(r,t)$ and Laplace radii, R_{Li}, located on substrates at the separation, D apart (Fig. 2), the augmented Young–Laplace equation for each drop is

$$-\frac{\sigma_{oi}}{r}\frac{\partial}{\partial r}\left(\frac{r\, z_{ir}}{(1+z_{ir}^2)^{1/2}}\right) = \frac{2\sigma_{oi}}{R_{Li}} - \Pi - p, i = 1 \text{ or } 2 \quad Drop-drop \tag{2.3.6}$$

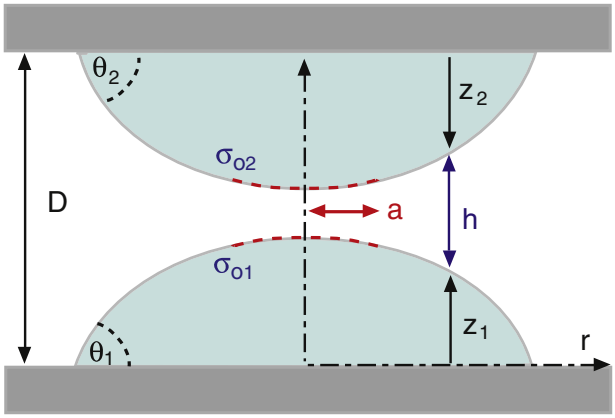

Fig. 2. Schematic diagram of the axisymmetric deformation within a small interaction zone of radius, a around the apex of two dissimilar drops interacting in a continuous phase.

Within the interaction zone defined by $r \sim a$, in which the slopes: $\partial z_i/\partial r = z_{ir} \ll 1$, $(i=1, 2)$, we can linearize Eq. (2.3.6) and use the geometric relation (Fig. 2)

$$z_1(r,t) + z_2(r,t) = D(t) - h(r,t) \tag{2.3.7}$$

to derive the equation for the film thickness, $h(r,t)$ between two drops

$$\frac{1}{2}\frac{\overline{\sigma}}{r}\frac{\partial}{\partial r}\left(r\frac{\partial h}{\partial r}\right) = \frac{2\overline{\sigma}}{\overline{R}} - (\Pi + p), 0 < r \sim a \quad Drop-drop \tag{2.3.8}$$

The constants $\overline{R}$ and $\overline{\sigma}$ are defined by

$$\frac{1}{\overline{R}} \equiv \frac{1}{2}\left(\frac{1}{R_{L1}} + \frac{1}{R_{L2}}\right) \text{ and } \frac{1}{\overline{\sigma}} \equiv \frac{1}{2}\left(\frac{1}{\sigma_{o1}} + \frac{1}{\sigma_{o2}}\right) \tag{2.3.9}$$

and are sometimes called the equivalent radius and equivalent interfacial tension. A factor (1/2) on the left hand side of Eq. (2.3.8) appears for this drop–drop case, when compared to Eq. (2.3.2a).

Eq. (2.3.8) can be integrated twice to give

$$h(r,t) \to h(0,t) + \frac{r^2}{\overline{R}} - 2\left(\frac{F(t)}{2\pi\overline{\sigma}}\right) log\left(\frac{r}{2\overline{R}_o}\right) + 2H(\overline{R}_o,t), r > a \quad Drop-drop \tag{2.3.10}$$

again a scale factor $\overline{R}_o \equiv 2/(1/R_{o1} + 1/R_{o2})$, defined in terms of the unperturbed radii of the two drops is used. An extra factor of 2 appears in the logarithm term in Eq. (2.3.10) when compared to the drop–particle result in Eq. (2.3.4).

Again the unknown quantities $h(0,t)$ and $H(\overline{R}_o,t)$ in Eq. (2.3.10) can be found by first solving Eq. (2.2.3) for the drop shape outside the interaction zone in Section 2.4 and then matching these to the inner solutions in Section 2.5.

2.4. Drop shape outside interaction zone

We study the shape of the drop outside the interaction zone, $r>a$, by starting with the solution of the Young–Laplace equation expressed in Eq. (2.2.3). To simplify the notation in this section, we define the quantities

$$G(t) \equiv \frac{F(t)}{2\pi\sigma_o} \text{ and } R \equiv R_L \tag{2.4.1}$$

Author's personal copy

where $G(t)$ has dimension of length and is a natural length scale for the size of the interaction zone. Thus Eq. (2.2.3) can be expressed in the simplified notation

$$r\sin\varphi = \frac{r^2}{R} - G(t), \quad \text{for } r \gg a. \tag{2.4.2}$$

Approaching the apex of the drop from outside towards the interaction zone, from Eq. (2.4.2) one observes that the tangent angle, $\varphi \to 0$, when $r \to (GR)^{1/2}$. Thus we can identify $a \equiv [FR/(2\pi\sigma_o)]^{1/2}$ as the radius of the interaction zone.

We can integrate the identity: $dz/dr = -\tan\varphi$ (Fig. 1), using the result

$$r = \frac{1}{2}R\left(\sin\varphi + \sqrt{\sin^2\varphi + 4G/R}\right) \tag{2.4.3}$$

obtained from solving Eq. (2.4.2), to give the height, $z(r)$ of the drop outside the interaction zone

$$z(r) = \int_\theta^\varphi \frac{dz}{dr}\frac{dr}{d\varphi}\,d\varphi = -\frac{1}{2}R\int_\theta^\varphi \sin\varphi\left(1 + \frac{\sin\varphi}{\sqrt{\sin^2\varphi + 4G/R}}\right)d\varphi \tag{2.4.4}$$

This result can be expressed in terms of elliptic integrals [32,36,37]. However, we will follow a different approach. Since we are only interested in the result for small forces that can be expressed as $(G/R) = F/(2\pi\sigma_o R) \ll 1$, the deviations of the contact angle: $\theta = \theta_o + \delta\theta$ and the Laplace radius $R = R_o + \delta R$ from their unperturbed values, θ_o and R_o, will be small. Therefore, we expand the lower limit of integration, θ and the integrand in Eq. (2.4.4) to linear order in $\delta\theta$, δR and G that results in

$$\begin{aligned} z(r) &= -R\int_{\theta_o}^{\varphi}\sin\varphi\,d\varphi + \{R_o\ \sin\theta_o\}\,\delta\theta + \left\{\int_{\theta_o}^{\varphi}\frac{1}{\sin\varphi}\,d\varphi\right\}G \\ &= R\,\cos\varphi\big|_{\theta_o}^{\varphi} + \{R_o\sin\theta_o\}\,\delta\theta - \left\{\frac{1}{2}\log\left(\frac{1+\cos\varphi}{1-\cos\varphi}\right)\Big|_{\theta_o}^{\varphi}\right\}G \end{aligned} \tag{2.4.5}$$

The shape of $z(r)$ near the apex of the drop can be found by using the approximations found from Eq. (2.4.2) and valid as $\varphi \to 0$:

$$\sin\varphi \approx \varphi + \ldots = \frac{r}{R} - \frac{G}{r} \tag{2.4.6a}$$

$$\cos\varphi \approx 1 - \frac{1}{2}\varphi^2 + \ldots = 1 - \frac{r^2}{2R^2} + \frac{G}{R} + O\left(G^2\right) \tag{2.4.6b}$$

Substituting these results into Eq. (2.4.5) and retaining only linear terms in $\delta\theta$, δR and G gives

$$\begin{aligned} z(r) \to R_o(1-\cos\theta_o) - \frac{r^2}{2R} + \{1-\cos\theta_o\}\ \delta R + \{R_o\ \sin\theta_o\}\,\delta\theta \\ + \left\{\log\left(\frac{r}{2R_o}\right) + 1 + \frac{1}{2}\log\left(\frac{1+\cos\theta_o}{1-\cos\theta_o}\right)\right\}G \end{aligned} \tag{2.4.7}$$

This is the form of the drop shape $z(r)$ as one approaches the interaction zone from the outside: $r \to a \equiv (GR)^{1/2}$, $\varphi \to 0$. The last terms that are independent of r represent changes to the drop height originating from the influence of the externally applied force.

In general, the various perturbation terms $\delta\theta$, δR and G do not vary independently. For example, if the drop maintains constant volume as it deforms there will be a condition that relates these terms. The volume of the drop, V_d is (integrating the outer solution, neglecting the small error of the interaction zone):

$$\begin{aligned} V_d &= \int_0^{z(0)}\pi r^2 dz = \int_\theta^0 \pi r^2\frac{dz}{dr}\frac{dr}{d\varphi}\,d\varphi \\ &= \frac{\pi R^3}{8}\int_0^\theta \frac{\left(\sin\varphi + \sqrt{\sin^2\varphi + 4G/R}\right)^3}{\sqrt{\sin^2\varphi + 4G/R}}\sin\varphi\ d\varphi \end{aligned} \tag{2.4.8}$$

Again expanding this result to linear order in $\delta\theta$, δR and G the constant volume constraint can be expressed as

$$\begin{aligned} \delta V_d &= \left(\frac{\partial V_d}{\partial\theta}\right)_o\delta\theta + \left(\frac{\partial V_d}{\partial R}\right)_o\delta R + \left(\frac{\partial V_d}{\partial G}\right)_o G \\ &= \left\{\pi R_o^3\ \ \sin^3\theta_o\right\}\ \delta\theta + \left\{\pi R_o^2\ (1-\cos\theta_o)^2(2+\cos\theta_o)\right\}\ \delta R \\ &\quad + \left\{\pi R_o^2(1-\cos\theta_o)\right\}\ G = 0 \end{aligned} \tag{2.4.9}$$

This provides a first relation between $\delta\theta$, δR and G. A second relationship between these three variables must originate from the way the drop responds to the external force. Two possibilities are that either the contact line remains fixed (pinned contact line or $r_1 =$ constant while θ_o changes, see Fig. 1) or the contact angle remains constant ($\theta_o =$ constant, while r_1 changes). These two possibilities will be explored in the next subsections.

2.4.1. A pinned contact line

For a contact line pinned at the radial position on the substrate $r_1 = R_o\sin\theta_o$ with $\varphi = \theta = \theta_o + \delta\theta$, (Fig. 1) we have from Eq. (2.4.2)

$$r_1^2 - r_1\ R\sin(\theta_o + \delta\theta) - R\ G = 0 \tag{2.4.10}$$

and to linear order in $\delta\theta$, $\delta R \equiv R - R_o$ and G this provides a second relation between $\delta\theta$, δR and G

$$\left\{\sin^2\theta_o\right\}\delta R + \{R_o\ \sin\theta_o\ \cos\theta_o\}\ \delta\theta + G = 0 \tag{2.4.11}$$

Thus the constant volume constraint, Eq. (2.4.9) and the pinned contact line condition, Eq. (2.4.11) enable us to express δR and $\delta\theta$ in terms of G

$$\delta R = \frac{-1}{(1-\cos\theta_o)}\ G,\ \ \delta\theta = \frac{1}{R_o\sin\theta_o}\ G. \tag{2.4.12}$$

The drop shape near the interaction zone: $\varphi \to 0$, $r \to a$ in Eq. (2.4.7) can now be expressed entirely in terms of the force, F, using Eq. (2.4.1):

$$z(r) = R_o(1-\cos\theta_o) - \frac{r^2}{2R_L} + \frac{F(t)}{2\pi\sigma}\left\{\log\left(\frac{r}{2R_o}\right) + 1 + \frac{1}{2}\log\left(\frac{1+\cos\theta_o}{1-\cos\theta_o}\right)\right\} \tag{2.4.13}$$

The first term on the RHS is the height of the undeformed drop, the second term is a local quadratic correction and the last term expresses the deformation due to the external force, $F(t)$ under a constant volume constraint and a pinned three phase contact line at the base of the drop.

2.4.2. A constant contact angle

For deformations at constant contact angle, θ_o, it is obvious that $\delta\theta = 0$ in Eq. (2.4.9) and the resulting relation between δR and G is

$$\delta R = \frac{-1}{(1-\cos\theta_o)(2+\cos\theta_o)}\ G \tag{2.4.14}$$

Author's personal copy

so from Eqs. (2.4.7) and (2.4.1), the drop shape near the interaction zone: $\varphi \to 0$, $r \to a$ for deformation under a constant contact angle is:

$$z(r) = R_o(1-\cos\theta_o) - \frac{r^2}{2R_L} + \frac{F(t)}{2\pi\sigma}\left\{ \log\left(\frac{r}{2R_o}\right) + 1 + \frac{1}{2}\log\left(\frac{1+\cos\theta_o}{1-\cos\theta_o}\right) - \frac{1}{2+\cos\theta_o}\right\} \tag{2.4.15}$$

This result differs from that in Eq. (2.4.13) in that the deformation due to the external force, $F(t)$ is under a constant volume constraint and a fixed contact angle at the base of the drop.

In summary, the outer shape of a deformed drop, $z(r,t)$ as one approaches the interaction zone, $r \to a$ from above has the form

$$z(r,t) \to R_o(1-\cos\theta_o) - \frac{r^2}{2R_L} + \frac{F(t)}{2\pi\sigma_o}\left\{ \log\left(\frac{r}{2R_o}\right) + B(\theta_o)\right\},\ r \to a \tag{2.4.16a}$$

where the function $B(\theta)$ depends on whether the drop deforms with a pinned three phase contact line at position r_1 or with a constant contact angle θ_o

$$B(\theta) \equiv \begin{cases} 1 + \frac{1}{2}\log\left(\frac{1+\cos\theta}{1-\cos\theta}\right) & \text{pinned } r_1 \\ 1 + \frac{1}{2}\log\left(\frac{1+\cos\theta}{1-\cos\theta}\right) - \frac{1}{2+\cos\theta} & \text{constant } \theta_0 \end{cases} \tag{2.4.16b}$$

Eqs. (2.4.10) to (2.4.16a), (2.4.16b) were derived previously by Bardos [51] using a more complicated approach. The advantage of the current approach is that it is more physically transparent and compact, without the need to resort to the use of elliptic integrals. Also, there is no need to treat acute and obtuse angles separately as was done in Bardos' work.

Before we match this result to the outer limiting form of the film thickness derived in Section 2.3, we examine the applicability of the constant volume constraint for the case of a deforming bubble.

2.4.3. Bubble compressibility

Assume that the internal pressure, P_{in} of the bubble containing N molecules in a volume, V_b obeys the ideal gas equation: $P_{in}V_b = NkT$, where k is Boltzmann's constant. If the Young–Laplace equation: $P_{in} = P_{out} + 2\sigma_o/R_o$ is valid, the volume is then:

$$V_b(R_o) = \frac{NkT}{\left(P_{out} + \frac{2\sigma_o}{R_o}\right)} \tag{2.4.17}$$

The variation of the bubble volume with regard to the change in the Laplace radius, δR, is

$$\delta V_b = \left(\frac{\partial V_b}{\partial R}\right)_o \delta R = \left\{\frac{V_b(R_o)}{R_o}\frac{2\sigma/R_o}{P_{out} + 2\sigma/R_o}\right\}\delta R \tag{2.4.18}$$

If the terms that contain $\cos\theta_o$ in Eq. (2.4.9) are of order unity, the magnitude of the coefficient of δR in Eq. (2.4.9) will be comparable to that of the coefficient of δR in Eq. (2.4.18) when $(2\sigma/R_o) \sim P_{out} \sim 1$ Bar. Thus for a bubble in water, bubble compressibility contributes about a 2% effect assuming a bubble radius of 70 μm.

2.5. Matching solutions for the force-displacement formula

We now match the limiting forms of the solutions of the film equation just beyond the interaction zone derived in Section 2.3 to the limiting form of the solution of the drop shape outside the interaction zone as one approaches the film from the outside obtained in Section 2.4.

2.5.1. Drop–sphere interaction

At the film boundary, $r \sim a$, we use the geometric condition in Eq. (2.3.1) to match the film solution given by Eq. (2.3.4) for the drop–sphere interaction with the drop shape solution given by Eqs. (2.4.16a)–(2.4.16b). The constant $[h(0,t) + H(R_{dso},t)]$ in Eq. (2.3.4) can be eliminated to give

$$h(r,t) \cong D(t) - R_o\ (1-\cos\theta_o) + \frac{r^2}{2R_{ds}} - \frac{F(t)}{2\pi\sigma_o}\left\{ \log\left(\frac{r}{2R_o}\right) + B(\theta_o)\right\}, r \sim a \tag{2.5.1}$$

The film radius for the drop–sphere interaction, a_{ds} can be taken to be the position where $\partial h/\partial r = 0$, and from Eq. (2.5.1), we find

$$a_{ds} \cong \left(\frac{F(t)R_{dso}}{2\pi\sigma_o}\right)^{1/2} \tag{2.5.2}$$

where, cf Eq. (2.3.2b)

$$\frac{1}{R_{dso}} \equiv \frac{1}{R_o} + \frac{1}{R_s} \tag{2.5.3}$$

is defined in terms of the undeformed drop radius, R_o and the sphere radius, R_s. On evaluating Eq. (2.5.1) at $r = a_{ds}$, we find

$$\Delta D(t) \equiv D(t) - R_o(1-\cos\theta_o) - h(a_{ds},t) \cong \frac{F(t)}{4\pi\sigma_o}\left\{ \log\left(\frac{F(t)R_{dso}}{8\pi\sigma_o R_o^2}\right) + 2B(\theta_o) - 1\right\} \tag{2.5.4}$$

An important observation is that this non-linear force-displacement relationship follows the Young–Laplace equation and implies that a drop or bubble does not behave as a Hookean spring under deformation as often assumed [14,52]. This result is also independent of the details of the repulsive disjoining pressure which determines the magnitude of the film thickness $h(a_{ds},t)$ that in practice is small compared to the displacement D. Consequently, for repulsive interactions, measuring the static or equilibrium force-displacement relationship will provide information about the interfacial tension σ_o, the drop radius R_o and the contact angle θ_o. However, the result will be insensitive to the detailed form of the repulsive disjoining pressure.

For force measurements using the atomic force microscope, Eq. (2.5.4) replaces the constant compliance condition as hard contact is no longer a valid concept when deformable drops are involved.

2.5.2. Drop–drop interaction

Again at the film boundary, $r \sim a$, we use the geometric condition in Eq. (2.3.7) to match the film solution given by Eq. (2.3.10) for the drop–drop interaction with the drop shape given by Eqs. (2.4.16a)–(2.4.16b). The constant $[h(0,t) + 2H(\bar{R}_o,t)]$ in Eq. (2.3.10) can be eliminated to give

$$h(r,t) \cong D(t) - R_{o1}\ (1-\cos\theta_{o1}) - R_{o2}\ (1-\cos\theta_{o2}) + \frac{r^2}{\bar{R}} - \frac{F(t)}{2\pi\sigma_{o1}}\left\{ \log\left(\frac{r}{2R_{o1}}\right) + B(\theta_{o1})\right\} - \frac{F(t)}{2\pi\sigma_{o2}}\left\{ \log\left(\frac{r}{2R_{o2}}\right) + B(\theta_{o2})\right\},\ r \sim a \tag{2.5.5}$$

The film radius for the drop–drop interaction, a_{dd} can be taken to be the position where $\partial h/\partial r = 0$, thus from Eq. (2.5.5)

$$a_{dd} \cong \left(\frac{F(t)\bar{R}_o}{2\pi\bar{\sigma}}\right)^{1/2} \tag{2.5.6}$$

Author's personal copy

where, cf Eq. (2.3.9)

$$\frac{1}{\overline{R}_o} \equiv \frac{1}{2}\left(\frac{1}{R_{o1}} + \frac{1}{R_{o2}}\right) \tag{2.5.7}$$

is defined in terms of the undeformed drop radii, R_{o1} and R_{o2}. On evaluating Eq. (2.5.5) at $r = a_{dd}$, we find

$$\begin{aligned}\Delta D(t) \equiv D(t) - R_{o1}(1-\cos\theta_{o1}) - R_{o2}(1-\cos\theta_{o2}) - h(a_{dd},t) \qquad (2.5.8)\\ \cong \frac{F(t)}{4\pi\sigma_{o1}}\left\{ log\left(\frac{F(t)\overline{R}_o}{8\pi\overline{\sigma}R_{o1}^2}\right) + 2B(\theta_{o1})\right\}\\ + \frac{F(t)}{4\pi\sigma_{o2}}\left\{ log\left(\frac{F(t)\overline{R}_o}{8\pi\overline{\sigma}R_{o2}^2}\right) + 2B(\theta_{o2})\right\} - \frac{F(t)}{2\pi\overline{\sigma}}\end{aligned}$$

which is the force, F *vs* displacement, D relation (see Fig. 2) for the interaction between two dissimilar deformable drops. The interfacial tensions, σ_{o1} and σ_{o2}, the contact angles, θ_{o1} and θ_{o2} and the undeformed drop radii, R_{o1} and R_{o2} can all be measured independently.

To recapitulate, the theoretical formulation in this work is valid when viscous forces are small compared to surface tension forces, that is, in the regime of small capillary number, and the interaction force is small as measured by the condition: $F/(2\pi\sigma_o R) \ll 1$. Under such circumstances, the size of the interaction zone, a between the drops is also small compared to the dimensions of the drop, R.

3. Hydrodynamic interactions

In non-equilibrium force measurement experiments, the relative motion between the interacting drops or between the drop and solid particle will generate hydrodynamic interactions that arise from the flow of the continuous phase. In experiments using the atomic force microscope (AFM) or the surface forces apparatus (SFA), the separation between the interacting bodies (h<1 μm) is small compared to the dimensions of the drops or particles (R~100 μm), so flow in the thin film between interacting bodies provides the dominant contribution to the measured non-equilibrium force. While the typical drive velocities used in AFM experiments (V~1–50 μm/s) span the range of Brownian velocities of the drops or particles, the Reynolds number, Re in water, is small ($Re = \rho RV/\mu < 10^{-2}$) so that a description based on Stokes flow is appropriate. Also the typical capillary number, Ca, the ratio of viscous forces to surface tension forces, is small ($Ca = \mu V/\sigma \sim 10^{-6}$) and justifies the use of the augmented Young–Laplace model to describe drop deformations.

A review of various treatments of hydrodynamic interactions will be the focus of this section.

3.1. Stokes–Reynolds lubrication theory

The description of fluid flow between thin deformable films in the low Reynolds number regime is as follows. Hydrodynamic flow in the deformable thin film trapped by the drop can be described using the lubrication theory [53,54]. Within this axisymmetric film comprised of a Newtonian liquid with shear viscosity μ, the dominant velocity component, $u(r,z,t)$ is in the radial r-direction and the pressure, p only varies in the r-direction. The velocity field is given by the radial component of the Stokes equations

$$\mu\frac{\partial^2 u(r,z,t)}{\partial z^2} = \frac{\partial p(r,t)}{\partial r} \tag{3.1.1}$$

Integration of the continuity equation from $z = 0$ to $h(r,t)$ together with the kinematics condition on the film surface gives the general evolution equation of the film thickness

$$\frac{\partial h(r,t)}{\partial t} = -\frac{1}{r}\frac{\partial}{\partial r}\left(r\int_0^{h(r,t)} u(r,z,t)dz\right) \tag{3.1.2}$$

Eq. (3.1.1) can be integrated with respect to z twice to find $u(r,z,t)$. In order to do so, hydrodynamic boundary conditions at the film surface ($z = 0$ and $z = h(r,t)$) must be specified. Substituting this solution into Eq. (3.1.2), gives an equation relating $h(r,t)$ and $p(r,t)$, that together with Eqs. (2.3.2a) or (2.3.8) provides a complete description of the evolution of the film (both spatial and temporal).

Different types of hydrodynamic boundary conditions at the surfaces of solids, drops and bubbles have been proposed. The appropriate choice will be guided by experimental conditions. For completeness, we summarize the film evolution equations corresponding to different boundary conditions.

The assumption at a solid–liquid interface is to require the fluid velocity at the interface to be the same as the velocity of the solid surface. This is referred to as the *no-slip* boundary condition. The analogous condition at a fluid–fluid interface is the *tangentially immobile* boundary condition in which the fluid velocity at such interfaces is also specified even though the interfaces can deform. This condition is regarded to be appropriate at interfaces populated by surface-active molecules that can arrest interfacial flow.

At ideal clean liquid–liquid or liquid–gas boundaries, the *fully mobile* condition whereby one assumes the continuity of the tangential components of the fluid velocity and of the tangential shear stress is expected to hold. This means it becomes necessary to match hydrodynamic flow inside and outside the drops. In lubrication flow, this gives rise to an additional integral equation involving the interfacial velocity that has to be solved (see Section 3.5).

The case of two interacting bubbles is of special interest because of its ubiquitous relevance in many areas of application. Theoretically, it is also a singular case in that if the fully mobile boundary condition is applied at the bubble interfaces, the thin film lubrication Eq. (3.1.1) will only admit a constant plug flow solution that provides no information about the hydrodynamic pressure. This led Chesters and Hofman [45] to include inertia effects in formulating their lubrication model. Although their numerical calculations also included the effects of bubble deformation, for non-deforming bubbles this model actually yields an infinite force between the bubbles (see Section 3.6). Such contradictory results stems from the fact that the lubrication formulation is not valid when inertial effects are dominant [54].

The effects of a non-uniform distribution of surface-active molecules being present at an interface will provide a surface tension gradient along the surface that can oppose the tangential hydrodynamic stress [55]. However, in such a model, it becomes necessary to consider convection and diffusion of such surface-active molecules during interaction (see Section 3.7).

Finally, the Stefan–Reynolds Flat Film Model [21,22] has been used for a long time to describe drop deformation and associated film drainage. In its original form it is attractive because simple analytic solutions are available (see Section 3.8). However, the unknown geometric parameters and inherent contradictory assumptions of the model mean that it lacks predictive capability. This model has spawned a number of modifications, which we call collectively *Neo Flat Film* models that involved additional assumptions and parameters with increasing mathematical complexity (see Section 3.9). In spite of such developments, the ability of this model in predicting experimental results is limited.

Author's personal copy

3.2. Non-deforming interfaces

The film thickness between two non-deforming solid spheres with radii R_a and R_b, is given by

$$h(r,t) = h_o(t) + \frac{r^2}{R_H}, \quad \frac{1}{R_H} \equiv \frac{1}{2}\left(\frac{1}{R_a} + \frac{1}{R_b}\right) \tag{3.2.1}$$

where the function $h_o(t)$ specifies how the spheres are moved relative to each other. The solution of the Stokes Eq. (3.1.1) with the *no-slip* boundary condition: $u=0$ at $z=0$ and $z=h(r,t)$ is

$$u(r,z,t) = -\frac{1}{2\mu}\frac{\partial p}{\partial r}\ z(h-z). \tag{3.2.2}$$

Combining Eqs. (3.1.2), (3.2.1) and (3.2.2), gives the film thinning equation

$$\frac{dh_o(t)}{dt} = \frac{1}{12\mu r}\frac{\partial}{\partial r}\left(r h^3 \frac{\partial p}{\partial r}\right) \tag{3.2.3}$$

This can be integrated to give

$$p(r,t) = -6\mu \frac{dh_o(t)}{dt} \int_r^\infty \frac{s\ ds}{[h(s,t)]^3} = -\frac{3\mu R_H}{2}\frac{dh_o(t)}{dt}\frac{1}{[h_o(t) + (r^2/R_H)]^2} \tag{3.2.4}$$

The pressure is defined to be zero outside the film and from Eq. (3.2.4) we see the pressure decays as $1/r^4$ as $r\to\infty$.

The hydrodynamic force, $F(t)$ acting between the spheres, in terms of the separation, $h_o(t)$ and the relative velocity, $dh_o(t)/dt$, is

$$F(t) = 2\pi \int_0^\infty r\ p(r,t) dr = -\frac{6\pi\mu R_H^2}{h_o(t)}\ \frac{dh_o(t)}{dt} \tag{3.2.5}$$

It is positive for a repulsive force as the spheres approach with $dh_o(t)/dt<0$ and it scales with the square of the drop radius, R_H^2.

If the spheres are driven together under a constant external force, F_{ext} (>0 for the spheres being pushed together) against hydrodynamic repulsion, the separation will decrease exponentially with time according to

$$h_o(t) = h_o(0)\exp(-t/\tau_{SS}) \tag{3.2.6}$$

with characteristic decay time for film drainage between the solid spheres

$$\tau_{SS} \equiv 6\pi\mu R_H^2 / F_{ext} \tag{3.2.7}$$

In this model, the spheres only come into contact as $t\to\infty$.

If an attractive non-retarded Van der Waals force with Hamaker constant, A expressed in the Derjaguin approximation

$$F_{VdW}(h) = -(\pi R_H)\frac{A}{12\pi h^2} \tag{3.2.8}$$

pulls the spheres together against the hydrodynamic repulsive force, the separation then varies with time according to

$$h_o(t) = h_o(0)(1-t/\tau_{VdW})^{1/2} \tag{3.2.9}$$

where the coalescence time, defined by $h_o(\tau_{VdW})=0$, is

$$\tau_{VdW} \equiv 36\pi\mu R_H [h_o(0)]^2 / A. \tag{3.2.10}$$

3.3. Tangentially immobile interfaces

For axisymmetric flow in the radial direction in a film with *tangentially immobile* boundaries, the boundary conditions are: $u=0$ at $z=0$ and $z=h(r,t)$ so the velocity has the same form as Eq. (3.2.2). However, when this is used in Eq. (3.1.2) we now have Stokes–Reynolds equation for the film thickness, $h(r,t)$

$$\frac{\partial h}{\partial t} = \frac{1}{12\mu r}\frac{\partial}{\partial r}\left(r h^3 \frac{\partial p}{\partial r}\right) \tag{3.3.1}$$

that has to be solved simultaneously with the Young–Laplace equation in either Eq. (2.3.2a) or (2.3.8) to obtain the hydrodynamic pressure, $p(r,t)$. The time-dependent force, $F(t)$ is then found using Eq. (2.2.2).

The numerical algorithm of the solution of the Stokes–Reynolds–Young–Laplace equations will be discussed in Section 4.

3.4. Navier slip interfaces

In the Navier slip model [56], the tangential component of the fluid velocity at an interface is taken to be proportional to the shear stress with a constant of proportionality called the slip length. It was postulated that this condition is appropriate for hydrophobic surfaces [57]. But the magnitude of the slip length required to match experiments was unrealistically large—in excess of 1 μm. There were also earlier reports of slip observed in dynamic force measurement between a solid particle and a flat surface using the atomic force microscope [58–60]. But subsequent refined measurements revealed that the "slip phenomenon" depended on the type of the force sensing cantilever used in the experiment [11–13,113].

For completeness, we give the film drainage equation between two solid surfaces that obey the Navier slip boundary condition with the possibility of different slip lengths b_o at $z=0$ and b_h at $z=h$. The resulting Stokes–Reynolds equation then has the form

$$\frac{\partial h}{\partial t} = \frac{1}{12\mu r}\frac{\partial}{\partial r}\left(r\ h^3\frac{\partial p}{\partial r}\right) + \frac{1}{4\mu r}\frac{\partial}{\partial r}\left(r\left[\frac{(b_o+b_h)h^3 + 4b_o b_h h^2}{h+b_o+b_h}\right]\frac{\partial p}{\partial r}\right) \tag{3.4.1}$$

It contains an additional term compared to the tangentially immobile model of Eq. (3.3.1). A classical "no-slip" condition will be obtained by setting both slip lengths to zero. If one surface (say 'h') belongs to that of an ideal bubble—with zero viscosity, whose surface cannot sustain any tangential shear stress, one can assume the limit $b_h\to\infty$. However, as we shall see in Section 3.6, we cannot obtain the result for film drainage between the surfaces of two such ideal bubbles from Eq. (3.4.1).

3.5. Two drops with mobile interfaces

If the interfaces of the interacting drops with internal viscosity μ_d, cannot sustain tangential stress, the solution of Eq. (3.1.1) will require the velocity $U(r,t)$ of the interface to be non-zero. Based on the continuity of the tangential stress across the interface, the following set of coupled equations must be used instead of Eq. (3.3.1) [23,61,62]:

$$\frac{\partial h}{\partial t} = \frac{1}{12\mu r}\frac{\partial}{\partial r}\left(r\ h^3\frac{\partial p}{\partial r}\right) - \frac{1}{r}\frac{\partial}{\partial r}(r\ h\ U) \quad \textit{mobile drops} \tag{3.5.1a}$$

$$U(r,t) = -\frac{1}{2\mu_d}\int_0^\infty \phi(r,\rho)\ h(\rho,t)\frac{\partial p(\rho,t)}{\partial \rho}\ d\rho \tag{3.5.1b}$$

Author's personal copy

$$\phi(r,\rho) = \frac{\rho}{2\pi}\int_0^{\pi} \frac{\cos\theta}{\sqrt{r^2+\rho^2-2r\rho\cos\theta}}\, d\theta \tag{3.5.1c}$$

The dimensionless number: $m \equiv (\mu/\mu_d)(R/h)^{1/2}$ [23,61] determines the behavior of the solution of the above equations. For $m \ll 1$, the interfaces tend towards tangential immobility, while for $m \gg 1$, the drainage rates are much faster and the dynamics of the system are mainly determined by the internal flow of the drops [63].

Other formulations for the drainage between drops with mobile interfaces exist that may appear simpler [64,65], but unfortunately the treatment of the flow field inside the drop is not correct. The correct account of mobile interfaces requires the use of an integral equation to couple the interfacial velocity to the shear stress [61].

3.6. Two bubbles: Chesters–Hofman model

If the interacting bubbles have fully mobile surfaces that cannot sustain shear stress, the solution to Eq. (3.2.2) that is valid for low Reynolds numbers, would be a constant plug flow velocity that provides no information on the pressure distribution. This led Chesters and Hofman [45] to consider the interaction between two identical deformable bubbles with mobile surfaces at high Reynolds numbers when viscosity effects of the fluid may be neglected. The Reynolds lubrication treatment was kept, while only inertial effects were included in their model. Eq. (3.1.1) was replaced by the equation for the plug flow velocity $U(r,t)$ in the radial direction of the film:

$$\frac{\partial U}{\partial t} + U\frac{\partial U}{\partial r} = -\frac{1}{\rho}\frac{\partial p}{\partial r} \tag{3.6.1}$$

with ρ the liquid density. The continuity equation now becomes

$$\frac{\partial h}{\partial t} = -\frac{1}{r}\frac{\partial}{\partial r}(r\ h\ U) \tag{3.6.2}$$

Assuming an initial film profile of $h(r,0) = h_o(t=0) + r^2/R_o$ with initial bubble radii, R_o these equations were solved numerically together with the Young–Laplace Eq. (2.3.8). The disjoining pressure was set to zero ($\Pi = 0$). The bubbles were assumed to approach with constant velocity, V.

If the bubbles do not deform, we will have $h_o(t) = h_{init} - Vt$, and Eq. (3.6.2) can be integrated to give the plug flow velocity

$$U(r,t) = \frac{Vr}{2\left[h_o(t) + r^2/R_o\right]} \tag{3.6.3}$$

The pressure, p can then be found from Eq. (3.6.1)

$$p(r,t) = \frac{\rho V^2 R_o^2}{8}\ \frac{\left[2h_o(t) + r^2/R_o\right]}{\left[h_o(t) + r^2/R_o\right]^2} \tag{3.6.4}$$

However, the resultant force, $F(t)$ between the bubbles, found by integrating this pressure

$$F(t) = 2\pi\int_0^{\infty} p(r',t)r'\ dr' \tag{3.6.5}$$

is infinite because the pressure in Eq. (3.6.4) does not decay fast enough as $r \to \infty$ for the integral in Eq. (3.6.5) to converge. The reason is that the lubrication equation failed to match to the full Navier–Stokes equation outside the thin film when only inertia effects are considered [54].

Chesters and Hofman [45] considered deformable bubbles for which only numerical solution of Eqs. (3.6.1) and (3.6.2) were given. They concluded that film rupture always occurs at the coalescence time

$$t_{CH} \cong \rho V R_o^2/\sigma. \tag{3.6.6}$$

without the need for any attractive surface forces. This time is measured from the moment at which the bubbles would have touched had deformation been absent. In contrast, the models discussed Sections 3.2–3.5, all require the presence of attractive surface forces [66] in order for film rupture to occur at a finite time. For 50 μm bubbles traveling at 50 μm/s, the predicted coalescence time of 10^{-9} s is much shorter than any experimental observations. Without further investigation, it is not clear if the divergence problem associated with the slow decay of the pressure field can be avoided by surface deformability.

In experiments on rising bubbles, the zero shear stress condition has been observed only when extreme care has been taken to de-ionise and clean the water [67–72]. However, when the same bubbles rise towards a solid surface such as a titania plate, their rate of approach suggested that the boundary condition at the bubble surface is again a tangentially immobile condition [73,74]. The precise physical reason for this behavior has yet to be established although trace impurities that originate from the titania plate or accumulated during bubble rise may be implicated.

Direct measurements of bubble–bubble interactions using the atomic force microscope suggest that trace surface-active impurities in the system are sufficient to render the bubbles to exhibit tangentially immobile interfaces even though extreme care has been taken to avoid such impurities (see Section 5). Thus it may be difficult in practice to achieve and maintain the level of cleanliness to guarantee the zero shear stress condition at bubble surfaces.

3.7. Bubbles with surface-active species

The presence of mobile surface-active molecules or transport processes associated with chemical reactions, material transport or temperature gradients can give rise to surface tension gradients. The corresponding boundary condition at such interfaces will be the continuity of the tangential components of the fluid velocities and a jump in the tangential shear stress across the interface balanced by the surface tension gradient [55]. These follow from kinematic and tangential force balance considerations. In addition, effects such as interfacial viscosity and surface elasticity have been proposed as being important when surfactants are present at interfaces. Theoretical considerations of these effects involve the introduction of model parameters that are difficult to determine independently. While such treatments modified the Stokes–Reynolds drainage equation, the corresponding effects on the derivation of the Young–Laplace equation had not been considered [75]. Consequently, a balanced approach is not available.

However as discussed in Section 3.6, there is experimental evidence that the presence of trace amounts of surface-active species would render an interface to be tangentially immobile so that the complex effects of surface-active species that have been postulated theoretically do not feature in dynamic force measurements.

3.8. Stefan–Reynolds Flat Film Model

The complexity of the Stokes–Reynolds–Young–Laplace model has led to the development of a number of approximate theories aimed at describing film drainage dynamics based on the Stefan–Reynolds Flat Film Model [21,22]. However, all these models fail to predict quantitative agreement when compared with experiments [76].

In spite of the inherent inconsistencies of the original model, numerous extensions and modifications have been proposed with new additional features. These extensions and modifications are not

Author's personal copy

always well justified from a physics point of view [77] and are not capable of producing the results solving the Stokes–Reynolds–Young–Laplace equations. We review these key issues in this section.

Consider the Stefan–Reynolds Flat Film Model of a drop (or bubble) approaching a flat solid surface. Instead of using the Young–Laplace equation to account for the deformation of the drop, the deformation is assumed to have the shape of a circular flat disk with radius, a (see Fig. 3). However, the dimension of the disk radius, a is not known *a priori*.

Assume that the drop approaches the surface due to an external time-dependent force, F_{ext}. The fluid in the film has a radial velocity, $u(r,z,t)$ (assuming axial symmetry and Stokes flow) and the film is now of uniform thickness, $h(t)$. At $z=0$ (the location of the solid surface), the boundary condition $u(r,0,t)=0$ is set. If the surface of the drop at $z=h$, is tangentially immobile, the condition $u(r,h,t)=0$ applies. If on the other hand the surface of the drop is assumed to have zero shear stress, then the condition $\partial u(r,z,t)/\partial z=0$ must be applied at $z=h$.

The pressure profile can be obtained from Eqs. (3.1.1) and (3.1.2) with the above boundary conditions as

$$p(r,t) = p_o - \frac{3\mu}{\beta h^3}\left(\frac{dh}{dt}\right)\left(a^2-r^2\right), 0<r<a \tag{3.8.1}$$

The pressure in the continuous phase, $r>a$, is represented by p_o, and μ is its viscosity. The constant β is taken to be $\beta=1$ if the flat surface of the drop is tangentially immobile and $\beta=4$ if the flat surface of the drop is fully mobile. This pressure profile gives rise to the hydrodynamic force (positive for repulsion between the drop and the flat surface)

$$F_{hydro} = 2\pi \int_0^a (p-p_o) r\,dr = -\frac{3\pi\mu a^4}{2\beta h^3}\left(\frac{dh}{dt}\right) \tag{3.8.2}$$

The quadratic pressure profile in Eq. (3.8.1) has a maximum at $r=0$ for an approaching drop with $dh/dt<0$ and decays monotonically to p_o at the outer film region ($r=a$). It presents us with an immediate inconsistency. Since the deformed interface of the drop is assumed to be a flat disk at the outset, then according to the Young–Laplace equation, the pressure on either side of such a flat interface must be equal. Therefore the quadratic pressure distribution given by Eq. (3.8.1) within the flat film is inconsistent with the uniform pressure inside the drop.

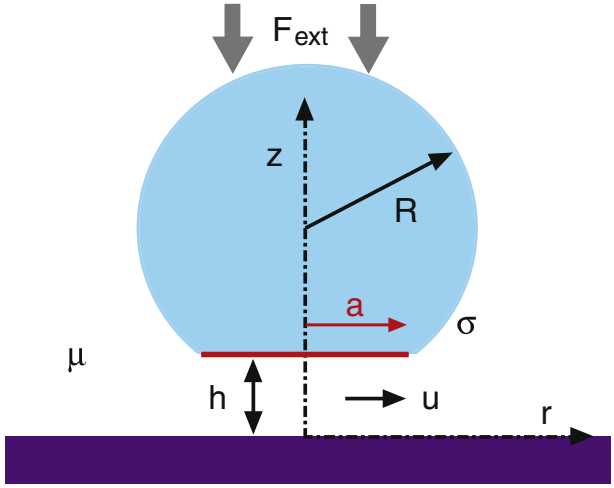

Fig. 3. Schematic diagram of the Stefan–Reynolds Flat Film Model for a drop or bubble with radius R, approaching a flat solid surface. The radius of the flat film region is a.

If we ignore this inconsistency for the time being and assume there is a disjoining pressure, $\Pi(h)$, acting on the film with area (πa^2), a quasi-static force balance on the drop in the z direction gives:

$$-F_{ext} + F_{hydro} + \left(\pi a^2\right)\Pi(h) = 0 \tag{3.8.3}$$

The external force F_{ext} is taken to be positive if it acts to push the drop towards the flat surface. This has been the starting point of modeling the stability of draining films under the action of Van der Waals forces [78].

A general prediction of the Stefan–Reynolds model is that a repulsive disjoining pressure will slow down the rate of drainage, dh/dt, according to Eq. (3.8.3). As we shall see in Section 5, this is opposite to experimental observations and predictions of the full solution of the Stokes–Reynolds–Young–Laplace equations.

3.9. Neo Flat Film models

Numerous experimental studies since the original experiment of Derjaguin and Kussakov [3] have demonstrated that real films are not flat. To accommodate such experimental evidence, there have been a number of attempts to develop corrections to the Reynolds Flat Film Model. All of these attempts involve simplifications of the Stokes–Reynolds partial differential equation given in Eq. (3.3.1) by making a set of assumptions that involve mathematical relations between the actual film thickness, $h(r,t)$ and the average film thickness, $h_{av}(t)$ defined by

$$h_{av}(t) \equiv \frac{2}{a^2}\int_0^a h(r,t) r\,dr \tag{3.9.1}$$

Here, the Reynolds film radius, a will also be time-dependent according to Eq. (3.8.3) if the external force is not constant. The following assumptions have been proposed:

(a) the "quasi-steady" assumption [75,79]:

$$\frac{\partial h(r,t)}{\partial t} \approx \frac{dh_{av}(t)}{dt}\,\frac{\partial h(r,t)}{\partial h_{av}(t)} \tag{3.9.2}$$

(b) the "homogeneous" assumption [79]:

$$\frac{\partial h(r,t)}{\partial h_{av}(t)} \approx \frac{h(r,t)}{h_{av}(t)} \tag{3.9.3}$$

(c) the assumption of small deviations from the average film thickness [79]:

$$[h(r,t)-h_{av}(t)]^2 << [h_{av}(t)]^2 \tag{3.9.4}$$

(d) the average thickness decays exponentially with time, t [79]

$$h_{av}(t) = h_{av}(0)e^{-bt} \tag{3.9.5}$$

where b and $h_{av}(0)$ are constants to be found by fitting to experimental data.

The assumptions given in Eqs. (3.9.1)–(3.9.5) are then used to reduce the Stokes–Reynolds–Young–Laplace coupled partial differential equations for the film thickness, $h(r,t)$ and the hydrodynamic pressure, $p(r,t)$:

$$\frac{\partial h}{\partial t} = \frac{1}{12\mu r}\frac{\partial}{\partial r}\left(r h^3 \frac{\partial p}{\partial r}\right) \tag{3.9.6}$$

Author's personal copy

$$\frac{\sigma}{2r}\frac{\partial}{\partial r}\left(r\frac{\partial h}{\partial r}\right)=\frac{2\sigma}{R_L}-\Pi(h)-p \tag{3.9.7}$$

for the case of two interacting identical drops with constant interfacial tension, σ and Laplace radius, R_L, to a single linear ordinary differential equation [79]

$$\frac{\sigma}{2}\Delta\Delta h(r,t)+\frac{\Pi(h_{av})}{\partial h_{av}}\Delta h(r,t)+\frac{12\mu V(t)}{h_{av}^4(t)}h(r,t)=0 \tag{3.9.8a}$$

$$\Delta\equiv\frac{1}{r}\frac{\partial}{\partial r}\left(r\frac{\partial}{\partial r}\right);\quad V(t)\equiv\frac{dh_{av}(t)}{dt} \tag{3.9.8b}$$

A number of papers and reviews have been devoted to obtain approximate solutions or analyze the behavior of this approximate linear equation [49,80–82]. However, the assumptions in Eqs. (3.9.2)–(3.9.5) have always been accepted without justification and certainly have not been tested by quantitative comparison with numerical solutions of the original Eqs. (3.9.6) and (3.9.7). For instance, the interpretation of the derivative $(\partial h/\partial h_{av})$ in Eq. (3.9.2) and the justification of Eq. (3.9.3) have not been established, and Eq. (3.9.5) is certainly not correct if a stable film can be formed. Thus in spite of numerous papers devoted to this approach to analyze film drainage, stability and coalescence its domain of validity is still very much an open question and appears to be a source of confusion [77].

4. Stokes–Reynolds–Young–Laplace model

In this section we summarize applications of the Stokes–Reynolds–Young–Laplace (SRYL) model to direct force measurements involving deformable drops. In particular, we give explicit forms of the governing equations and boundary conditions that need to be solved. We also outline perturbation solutions that can reveal the key physics of the problem even though the results are only applicable for weak interactions.

In a force measurement experiment with the atomic force microscope (AFM), the force, F between two objects is obtained from the deflection, S of a cantilever with calibrated spring constant, K: $F=KS$, by varying the position X of the cantilever (Fig. 4). The absolute separation, h between interacting rigid objects is inferred from the so-called constant compliance region when the two object are in hard contact when the condition: $\Delta S=\Delta X$ holds. As a result, F *vs* ΔX data can be converted to F *vs* h information.

For interactions involving deformable drops, the concept of hard contact no longer exists as the drops can deform. However, we can derive analytic formulae for interacting drop–sphere and drop–drop configurations to replace the constant compliance condition for interacting rigid objects. Details of implementations of numerical solutions of the governing equations that will facilitate quantitative comparisons between theory and experiments are also discussed.

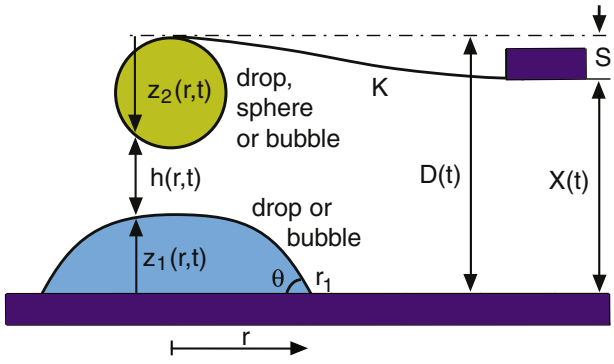

Fig. 4. The geometry of the atomic force microscope in which the distances D and X are defined.

4.1. Governing equations and boundary conditions

For the Stokes–Reynolds film drainage equation, we will consider in detail only the case for which the tangentially immobile boundary condition holds at the film boundaries. This is guided by the fact that all experimental results that we have gathered in this review are found to be consistent with this condition (see Section 5). In the domain $0<r<r_{max}$ that contains all detailed information about interactions involving the deformable film we solve the Stokes–Reynolds equation (see Eq. (3.3.1)) that relates the rate of the change of the film thickness, $h(r,t)$ to the hydrodynamic pressure, $p(r,t)$:

$$\frac{\partial h}{\partial t}=\frac{1}{12\mu r}\frac{\partial}{\partial r}\left(rh^3\frac{\partial p}{\partial r}\right) \tag{4.1.1}$$

For numerical calculations, the choice of r_{max} will be discussed in Section 4.5. For the axisymmetric interactions considered here, we apply the symmetry conditions: $\partial h/\partial r=0=\partial p/\partial r$ at $r=0$. As r approaches r_{max}, we see from Eqs. (2.3.4) and (2.3.10) that the film thickness, h increases with a quadratic dependence in r which will result in a pressure that decays like r^{-4}, see Eq. (3.2.3). This asymptotic pressure behavior can be implemented as the condition: $r(\partial p/\partial r)+4p=0$ at $r=r_{max}$.

The time-dependent force can be calculated using Eq. (2.2.2). In a numerical implementation, we use

$$F(t)\cong 2\pi\int_0^{r_{max}}[p(r',t)+\Pi(r',t)]r'\,dr'+2\pi\int_{r_{max}}^{\infty}p(r',t)r'\,dr' \tag{4.1.2}$$

since the disjoining pressure Π is short-ranged and is negligible for $r>r_{max}$, and the second integral can be evaluated analytically using the r^{-4} dependence of the pressure expressed in the form: $p(r,t)\approx p(r_{max},t)\,(r_{max}/r)^{-4}$, for $r>r_{max}$.

The Young–Laplace equation provides a second equation between the film thickness, $h(r,t)$ and the pressure, $p(r,t)$. As discussed in Section 2, this equation takes on different forms for drop–sphere or drop–drop interactions. To simplify the notation, we define a constant n

$$n=\begin{cases}1, & Drop-Sphere\\ 2, & Drop-Drop\end{cases} \tag{4.1.3}$$

We only consider drops with constant interfacial tensions for which the Young–Laplace equation can be written as

$$\frac{1}{n}\frac{\sigma_n}{r}\frac{\partial}{\partial r}\left(r\frac{\partial h}{\partial r}\right)=\frac{2\sigma_n}{R_n}-\Pi-p \tag{4.1.4}$$

with the equivalent surface tension and equivalent radius defined as:

$$\sigma_n=\begin{cases}\sigma_o, & Drop-Sphere\\ 2\,(1/\sigma_{o1}+1/\sigma_{o2})^{-1}, & Drop-Drop\end{cases} \tag{4.1.5}$$

$$R_n=\begin{cases}(1/R_o+1/R_s)^{-1}, & Drop-Sphere\\ 2\,(1/R_{o1}+1/R_{o2})^{-1}, & Drop-Drop\end{cases} \tag{4.1.6}$$

where the drops have constant interfacial tensions: σ_o, σ_{o1} and σ_{o2}, undeformed radii: R_o, R_{o1} and R_{o2}, and the solid sphere has radius: R_s. The interaction between a drop and a flat plate corresponds to the limit $R_s\to\infty$. As long as the deformations of the drops are small compared to the drop size, a condition that is well satisfied, we can approximate the Laplace radii by the undeformed radii of the drops in Eq. (4.1.4).

Author's personal copy

The initial film thickness is taken to be that between unperturbed drops and has the form:

$$h(r,0) = h_{init} + \frac{n r^2}{2R_n} \tag{4.1.7}$$

To solve the Stokes–Reynolds–Young–Laplace Eqs. (4.1.1) and (4.1.4) we need one more boundary condition. In non-equilibrium force measurements using the AFM, the displacement, $X(t)$ of the end of the force sensing cantilever (Fig. 4) determines the type of collision that the drops will experience and provides the final boundary condition at r_{max}.

The interaction force, F between a deformable drop and a sphere is related to the cantilever deflection, $S = F/K$ where K is the cantilever spring constant. The final boundary condition can be found by differentiating the outer asymptotic form of the film thickness, Eq. (2.5.1), with respect to time, t and use the geometric relation $D = S + X$ (see Fig. 4) to give, at $r = r_{max}$

$$\frac{\partial h(r_{max},t)}{\partial t} = \frac{dX(t)}{dt} + \frac{1}{K}\frac{dF(t)}{dt} - \frac{1}{2\pi\sigma_o}\frac{dF(t)}{dt}\left\{ log\left(\frac{r_{max}}{2R_o}\right) + B(\theta_o)\right\} \quad Drop–Sphere \tag{4.1.8}$$

The function $B(\theta)$ is defined by Eq. (2.4.16b).

We note that in previous work [48,62], only the first term on the RHS of Eq. (4.1.8) is used in the so-called "constant velocity" boundary condition. The second term on the RHS of Eq. (4.1.8) accounts for the deformation of the drop outside the film as well as the effect of the deflection of the AFM cantilever.

For the interaction between two drops we differentiate the corresponding asymptotic formula in Eq. (2.5.5) to give the required boundary condition at $r = r_{max}$

$$\frac{\partial h(r_{max},t)}{\partial t} = \frac{dX(t)}{dt} + \frac{1}{K}\frac{dF(t)}{dt} - \frac{1}{2\pi\sigma_{o1}}\frac{dF(t)}{dt}\left\{ log\left(\frac{r_{max}}{2R_{o1}}\right) + B(\theta_{o1})\right\} - \frac{1}{2\pi\sigma_{o2}}\frac{dF(t)}{dt}\left\{ log\left(\frac{r_{max}}{2R_{o2}}\right) + B(\theta_{o2})\right\} \quad Drop–Drop \tag{4.1.9}$$

The last 3 terms on the RHS of Eq. (4.1.9) are contributions to the boundary condition due to deflection of the cantilever and deformations of the drops outside the interaction zone.

We have now specified all the governing equations and appropriate boundary conditions that are necessary to model non-equilibrium force measurement using the AFM.

4.2. Scaled equations for computations

With appropriate scaling, the Stokes–Reynolds–Young–Laplace equations have a general form from which general features of the solution can be extracted. To illustrate the approach, we consider interactions in a force measurement experiment with the atomic force microscope where the displacement function, $X(t)$ of the end of the force-sensing cantilever is specified as a function of time and the force will vary. We also consider interactions at constant force where the relative velocity will vary with time.

4.2.1. Interaction under given displacement function

Let V be a characteristic value of the piezo drive velocity, $dX(t)/dt$ of the atomic force microscope. The ratio of viscous forces to surface tension forces is characterized by the capillary number $Ca \equiv \mu V/\sigma_n$. For the experimental systems considered here, $Ca \sim 10^{-6}$.

Non-dimensionalization of the SRYL equations leads to a universal form of the system of equations with the following scaling parameters [83]:

film thickness: h, $z \sim Ca^{1/2}R_n$,
radial coordinate: $r \sim Ca^{1/4}R_n$,
time: $t \sim Ca^{1/2}R_n/V$,
pressure: $p \sim \sigma_n/R_n$ and
force: $F \sim Ca^{1/2}\,\sigma_n\,R_n$.

The Stokes–Reynolds equation that describes film drainage between two drops with immobile interfaces, Eq. (4.1.1), becomes (using asterisks for dimensionless variables),

$$\frac{\partial h^*}{\partial t^*} = \frac{1}{12 r^*}\frac{\partial}{\partial r^*}\left(r^*\ h^{*3}\frac{\partial p^*}{\partial r^*}\right) \tag{4.2.1}$$

while the Young–Laplace Eq. (4.1.4) becomes

$$\frac{1}{n}\frac{1}{r^*}\frac{\partial}{\partial r^*}\left(r^*\frac{\partial h^*}{\partial r^*}\right) = 2 - \Pi^* - p^* \tag{4.2.2}$$

with $\Pi^* \equiv (R_n/\sigma_n)\Pi$. The initial condition in Eq. (4.1.7) becomes

$$h^*(r^*,0) = h_o^* + \frac{n(r^*)^2}{2}. \tag{4.2.3}$$

Apart from the scaled disjoining pressure, these equations contain no parameters. The boundary condition at r^*_{max}, given by Eqs. (4.1.8) or (4.1.9), has only a weak logarithmic dependence on the capillary number Ca

$$\frac{\partial h^*\left(r^*_{max},t^*\right)}{\partial t^*} = \frac{dX^*}{dt^*} - \frac{1}{2\pi}\frac{dF^*}{dt^*}\left\{ log\left(\frac{Ca^{1/4}R_n\ r^*_{max}}{2\ R_o}\right) + B(\theta_o)\right\} \quad Drop–Sphere \tag{4.2.4}$$

$$\frac{\partial h^*\left(r^*_{max},t^*\right)}{\partial t^*} = \frac{dX^*}{dt^*} - \frac{\sigma_n}{2\pi\ \sigma_{o1}}\frac{dF^*}{dt^*}\left\{ log\left(\frac{Ca^{1/4}R_n\ r^*_{max}}{2\ R_{o1}}\right) + B(\theta_{o1})\right\} - \frac{\sigma_n}{2\pi\ \sigma_{o2}}\frac{dF^*}{dt^*}\left\{ log\left(\frac{Ca^{1/4}R_n\ r^*_{max}}{2\ R_{o2}}\right) + B(\theta_{o2})\right\} \quad Drop–Drop \tag{4.2.5}$$

where $dX(t)/dt \equiv V\ dX^*(t^*)/dt^*$. For the case of two identical drops, numerical solutions of these equations in the absence of a disjoining pressure, $\Pi = 0$, and for a constant approach velocity: $dX(t)/dt = -V$ [84] revealed that the film profile will first exhibit a dimple when the central separation reaches the value

$$h(r=0,t) = cR_nCa^{1/2} \equiv h_{dimple} \tag{4.2.6}$$

In Eq. (4.2.6), c is a constant ranging from about 0.3 for $Ca \sim 10^{-10}$ to about 0.5 for $Ca \sim 10^{-4}$. Erroneously, in Manica et al. [84] and Chan et al. [85] the corresponding constant quoted for h_{dimple} was for a drop against a solid plate, namely, ~0.4 for $Ca \sim 10^{-10}$ and ~0.7 for $Ca \sim 10^{-4}$. The maximum shear stress for the above drop–drop case is about $\tau_{max} \sim 0.5Ca^{1/4}\sigma_n/R_n$ and occurs at the rim position, $r_{rim} \sim 3\ Ca^{1/4}R_n$. It takes about $t \sim 50\ Ca^{1/2}R_n/V$ for the thickness at the rim to drain from h_{dimple} to half this value.

4.2.2. Interaction under constant force

The constant force case corresponds to $dF/dt = 0$. This can be modeled by choosing a convenient constant velocity $dX(t)/dt = -V$ and monitor the force, $F(t)$ until it reaches the desired value, F_o, at some time $t = t_o$, and then set $dX(t)/dt = 0$ for $t > t_o$. Assuming the disjoining pressure is negligible ($\Pi \sim 0$), a 'universal set of equations

Author's personal copy

containing no parameters at all' [83] appears again using the scaling parameters:

film thickness: h, $z \sim F_o/\sigma_n$,
radial coordinate: $r \sim (F_o\, R_n/\sigma_n)^{1/2}$,
time: $t \sim \mu R_n^2/F_o$ and
pressure: $p \sim \sigma/R_n$

For this case, the dimple in the film will first appear at the separation

$$h(r=0,t) = 0.08(F_o/\sigma_n) \equiv h_{dimple} \tag{4.2.7}$$

The maximum shear stress of $\tau_{max} \sim 0.25\ (F_o\, \sigma_n/R_n^3)^{1/2}$ is reached just after the time of dimple formation and is located around the rim region of the film. As film drainage proceeds, the shear stress gradually diminishes. For $t > 200\ \mu R_n^2/F_o$, the rim radius reaches a constant value $r_{rim} \sim 0.375\ (F_o\, R_n/\sigma_n)^{1/2}$. The rim reduces to ½ h_{dimple} around $t \sim 100\ \mu R_n^2/F_o$ and to about 0.1 h_{dimple} at $t \sim 1000\ \mu R_n^2/F_o$ exhibiting an asymptotic time dependence of $t^{-2/3}$ [23].

4.3. Perturbation solutions

The Stokes–Reynolds–Young–Laplace (SRYL) Eqs., (4.1.1) and (4.1.4) form a pair of coupled partial differential equations that can only be solved numerically. Nonetheless, some of the key physics of non-equilibrium interactions involving deformable drops can be extracted by considering a perturbation solution of the SRYL equations. Such solutions have been found for axisymmetric interactions between drops driven together under constant force [23] and also for drop–drop interactions in the Hele–Shaw microfluidic channel geometry [91].

We remark that although the derivation of the different forms of the augmented Young–Laplace equation, Eqs. (2.3.2a) and (2.3.8), already involved a linearization in the drop shape, the resulting equations are still non-linear functions of the film thickness, h because of the presence of the hydrodynamic pressure, p and disjoining pressure, $\Pi(h)$. In addition, the Stokes–Reynolds equation that describes film thinning, Eq. (3.3.1) is also non-linear in h.

4.3.1. Axisymmetric drops

First we summarize results for the case of two identical axisymmetric drops with interfacial tension, σ_o and undeformed radius, R_o. Both drops are assumed to rest on flat substrates with contact angle, θ and the substrates are driven at relative velocity $V(t) > 0$ for separating drops. We seek solutions for the film thickness and pressure of the form

$$h(r,t) \equiv h_o(r,t) + h_1(r,t) \tag{4.3.1}$$

$$p(r,t) \equiv p_o(r,t) + p_1(r,t) \tag{4.3.2}$$

by choosing the parabolic profile $h_o(r,t) \equiv H(t) + r^2/R_o$ as the reference shape. The perturbations $h_1(r,t)$ and $p_1(r,t)$ are found by substituting Eqs. (4.3.1) and (4.3.2) into (4.1.1) and (4.1.4) and retaining only linear terms in h_1 and p_1. The solution, in the absence of a disjoining pressure is [85]

$$h(r,t) = H(t) + r^2/R_o + \left(\frac{3\mu R_o^2 V(t)}{4\sigma_o H(t)}\right)\left\{ log\left(\frac{H(t) + r^2/R_o}{4R_o}\right) + 2B(\theta)\right\} \tag{4.3.3}$$

with $H(t) = H_o + \int_0^t V(\tau)\, d\tau$. This perturbation solution is valid when the film capillary number, $Ca_f \sim (\mu V_o/\sigma_o)(R_o/H_o)^2 \ll 1$, with V_o being the characteristic velocity. The term in braces in Eq. (4.3.3) is negative so that the deformation $h_1(r,t)$ and the parabolic profile $h_o(r,t)$ have opposite signs. This has two physical implications.

For approaching drops corresponding to $V(t) < 0$, the perturbation will cause the central separation to thicken and this is the physical origin of dimple formation. The perturbation solution predicts a critical central film thickness $h_{dimple} \sim \alpha\ Ca^{1/2} R_o$ at which dimple formation will occur at constant velocity. However, when compared to numerical solutions of the SRYL equations, the constant α is too large by an order of magnitude. This is perhaps not surprising since dimple formation actually occurs at separations where non-deforming drops would have overlapped, a regime beyond the validity of the first order perturbation result above.

For separating drops corresponding to $V(t) > 0$ and the central separation, $H(t)$ increasing with time, the perturbation $h_1(r,t)$ will initially be negative and decreases the central film thickness. For sufficiently large film capillary number Ca_f, the initial decrease in central film thickness can bring the separation down to the range where the de-stabilizing influence of Van der Waals attraction can take hold and initiate coalescence. Such coalescence on separation phenomenon has been observed experimentally [25,86–90].

The deformation behavior under constant force conditions (e.g. due to buoyancy) has also been studied by perturbation methods. The result shows that the central separation evolves with an exponential dependence on time under a constant external force, F_{ext} [23,85]:

$$H(t) = H_o \exp\left[\left(2F_{ext}/3\pi\mu R_o^2\right)t\right] \tag{4.3.4}$$

4.3.2. Drops in the microfluidic Hele–Shaw cell geometry

The film thickness, $h(x,t)$ and the pressure, $p(x,t)$ for two interacting pancake-shaped drops in the Hele–Shaw cell geometry are determined by the following coupled equations in the absence of a disjoining pressure [91]

$$\frac{\partial h}{\partial t} = \frac{1}{3\mu}\frac{\partial}{\partial x}\left(h^3\frac{\partial p}{\partial x}\right) \tag{4.3.5}$$

$$\sigma_o \frac{\partial^2 h}{\partial x^2} = \frac{\sigma_o}{R_o} - p \tag{4.3.6}$$

in which the spatial coordinate x is transverse to the axis of symmetry. Again, the tangentially immobile hydrodynamic boundary condition has been assumed at the drop interface. The simpler form of the SRYL equation in the Hele–Shaw geometry means that the asymptotic analysis discussed in Section 2 can be carried out relatively easily [92].

The natural perturbation parameter is the capillary number in Hele–Shaw geometry: $Ca_{HS} \sim (\mu V_o/\sigma_o)(R_o/H_o)^{3/2}$ which differs from that of the axisymmetric case by a 3/2-power dependence on the aspect ratio (R_o/H_o). However, the effects of the perturbation term due to deformations of approaching or separation drops are qualitatively the same as in the axisymmetric case.

4.4. Force-displacement formula for AFM experiments

In AFM force measurement experiments involving rigid bodies, the absolute separation can be inferred from the constant compliance regions of the force *vs* cantilever displacement response that occurs when the two interacting bodies come into hard contact. For interactions involving deformable drops, hard contact does not occur as the drops can deform. In place of this limiting behavior, we can use the geometric relation in the AFM for a drop–sphere interaction (Fig. 4): $D(t) = X(t) + S(t)$, where the cantilever deflection $S(t) = F(t)/K$ is related to the force, F and cantilever spring constant, K by Hooke's law. Thus using the result in Eq. (2.5.4) we have the result

Author's personal copy

that replaces the constant compliance condition for the drop–sphere interaction

$$\Delta X(t) \cong \frac{F(t)}{4\pi\sigma_o}\left\{ log\left(\frac{F(t)R_{dso}}{8\pi\sigma_o R_o^2}\right) + 2B(\theta_o) - 1 - \frac{4\pi\sigma_o}{K}\right\} \quad Drop-Sphere \tag{4.4.1}$$

The function $B(\theta)$ is defined earlier in Eq. (2.4.16b). At low driving velocities, small dX/dt, this relation is valid for the entire force range. At higher driving velocities, this relation is valid when the force is sufficiently large. In Section 5, we will see an example of how this result can be applied in practice.

Similarly for AFM force measurements between two dissimilar deformable drops, we use the result in Eq. (2.5.8) to give

$$\Delta X(t) \cong \frac{F(t)}{4\pi\sigma_{o1}}\left\{ log\left(\frac{F(t)\overline{R}_o}{8\pi\overline{\sigma}R_{o1}^2}\right) + 2B(\theta_{o1})\right\} + \frac{F(t)}{4\pi\sigma_{o2}}\left\{ log\left(\frac{F(t)\overline{R}_o}{8\pi\overline{\sigma}R_{o2}^2}\right) + 2B(\theta_{o2})\right\} - \frac{F(t)}{2\pi\overline{\sigma}}\left\{1 + \frac{2\pi\overline{\sigma}}{K}\right\} \quad Drop-Drop \tag{4.4.2}$$

This is a generalization of a similar result given earlier for drops with the same interfacial tension [93]. Unfortunately that result contained a typographical error.

Both Eqs. (4.4.1) and (4.4.2) are very useful for checking the large force limit of experimental force *vs* cantilever results as well as for checking numerical solutions of the Stokes–Reynolds–Young–Laplace equations. They are applicable in the regime when the interacting drops have been pushed together at the separation below which they would overlap if they had not deformed.

4.5. Numerical algorithm

In this section, we give details on how to solve the scaled non-dimensional Stokes–Reynolds–Young–Laplace equations derived in Section 4.2:

$$\frac{\partial h^*}{\partial t^*} = \frac{1}{12r^*}\frac{\partial}{\partial r^*}\left(r^*\ h^{*3}\frac{\partial p^*}{\partial r^*}\right) \tag{4.5.1}$$

$$\frac{1}{n}\frac{1}{r^*}\frac{\partial}{\partial r^*}\left(r^*\frac{\partial h^*}{\partial r^*}\right) = 2 - \Pi^* - p^* \tag{4.5.2}$$

with the initial condition,

$$h^*(r^*,0) = h_o{}^* + \frac{n(r^*)^2}{2} \tag{4.5.3}$$

boundary conditions at $r^* = 0$

$$\frac{\partial h^*}{\partial r^*} = 0 = \frac{\partial p^*}{\partial r^*} \tag{4.5.4}$$

and at $r^* = r^*{}_{max}$

$$r^*\frac{\partial p^*}{\partial r^*} + 4p^* = 0 \tag{4.5.5}$$

$$\frac{\partial h^*(r^*_{max},t^*)}{\partial t^*} = \frac{dX^*(t^*)}{dt^*} + \Phi_n(r^*_{max})\frac{dF^*(t^*)}{dt^*} \tag{4.5.6}$$

where $\Phi_n(r^*{}_{max})$ the coefficient of dF^*/dt in Eq. (4.2.4) for drop–sphere ($n=1$) or Eq. (4.2.5) for drop–drop ($n=2$) interactions. The scaled force is given by Eq. (4.1.2) after using the $1/r^4$ asymptotic form for the pressure for $r^* > r^*{}_{max}$:

$$F^*(t^*) \cong 2\pi \int_0^{r^*_{max}} [p^*(r',t^*) + \Pi^*(r',t^*)]r'\ dr' + \pi\ (r^*_{max})^2\ p^*(r^*_{max},t^*) \tag{4.5.7}$$

The pressure p^* can be eliminated between Eqs. (4.5.1) and (4.5.2) to obtain an equation for $\partial h^*/\partial t^*$. The r-derivatives of the resulting equation can be discretized using central differencing in $[0, r^*_{max}]$ to obtain a set of coupled differential equations for $H_k(t^*) \equiv h^*(k\ \Delta r, t^*)$, $k = 0, .., N$ and $\Delta r = r^*_{max}/N$. The function $F^*(t^*)$ is related to all the $H_k(t^*)$ via Eq. (4.5.7) where the integral can be evaluated by Simpson's rule and can be written as:

$$F^*(t^*) = \sum_k w_k\ g(H_k(t^*)) \tag{4.5.8}$$

The system of coupled first order equations for the time derivative $dH_k(t^*)/dt^* \equiv \dot{H}_k(t^*)$ then has the form

$$\begin{pmatrix} 1 & 0 & .. & 0 & 0 \\ 0 & 1 & 0 & .. & 0 \\ & & \vdots & & \\ 0 & 0 & .. & 1 & \Phi_n \\ 0 & 0 & .. & 0 & 0 \end{pmatrix} \begin{pmatrix} \dot{H}_0 \\ \dot{H}_1 \\ \vdots \\ \dot{H}_N \\ \dot{F}^* \end{pmatrix} = \begin{pmatrix} f_0 \\ f_1 \\ \vdots \\ dX^*/dt^* \\ F^* - \sum_k w_k g(H_k) \end{pmatrix} \tag{4.5.9}$$

where f_k represent the terms resulting from the discretization in r corresponding to each equation for $dH_k(t^*)/dt^*$. This system has a singular mass matrix and is a differential-algebraic equation. It can be solved using standard software routines such as ODE15S in Matlab.

Once the driving function dX/dt is specified, Eq. (4.5.9) can be solved for $t > 0$. In actual implementations, to obtain numerical answers that are independent of domain size to 5 significant figures we choose a domain size $r_{max}{}^* = 10$, with a step size $\Delta r^* = 0.02$ which produces a system of 500 equations. A complete force curve can be computed in about 1 min on a notebook computer.

5. Comparisons with experiments

We complete this review by showing how the Stokes–Reynolds–Young–Laplace (SRYL) model can be applied to understand the dynamic behavior in different types of non-equilibrium experiments. We demonstrate in Section 5.1 that the SRYL model can make accurate quantitative predictions about the evolution of the shape of deformable films trapped between drops or bubbles as they undergo non-equilibrium interactions with solid surfaces or with other drops. In Section 5.2, we compare non-equilibrium force measurements involving drops and bubbles using the atomic force microscope (AFM) with predictions of the SRYL model. Once the SRYL model is shown to be able to give an accurate account of time variations of the non-equilibrium forces, we can confidently use the model to infer the spatial and temporal evolutions of the shape of the film between interacting drops and bubbles for interactions that result in film stability or coalescence. The availability of a quantitative theory overcomes one of the limitations of the experimental methods based on the AFM, namely that at present, the film profile between interacting drops cannot be observed directly.

In all systems that we have considered, the disjoining pressure contains only contributions from Van der Waals and electrical double layer interactions in the DLVO theory [1,2]. To calculate the Van der Waals interaction where it is dominant in bubble–bubble coalescence studies at high salt concentrations, we use the full Lifshitz theory [94] with the most complete dielectric data available. In experiments where the electrical double layer repulsion is dominant, we use the full non-linear Poisson–Boltzmann theory to calculate the disjoining

Author's personal copy

pressure. Values of the surface potentials and electrolyte concentrations are taken from independent experimental measurements.

5.1. Dynamic deformations

In this section, we highlight examples of experiments that measure the non-equilibrium shapes of drops and bubble during drop–drop, bubble–solid and drop–solid interactions. We compare predictions of the SRYL model with such non-equilibrium experiments.

5.1.1. Opposing protuberant drops

In this experiment, the interaction is between opposing protuberant half drops of glycerol that have emerged from the ends of two sealed capillaries (3 mm diameter) in silicone oil 47V300. The drops have an initial radius of $R_o = 1.52$ mm, while the interfacial tension for this system is $\sigma_o = 30$ mN/m. The drops are attached to the capillaries with a contact angle, $\theta = 90°$ [48,84]. The drops were driven together from rest at an initial large separation, by mechanically moving one capillary towards the second with a constant velocity, $V = 6.7$ μm/s. Setting the time $t = 0$ to the time when the two drops would have touched if they would not have deformed, the approach was stopped at $t_{stop} = 27$ s. The fringes obtained with a laser-induced interference pattern were used to measure the film thickness profile, $h(r,t)$ as a function of position and time.

A comparison of the measured and predicted fringe pattern just at the time when the drive stopped is shown in Fig. 5, together with samples of the film thickness $h(r,t)$ at earlier times. Note that a dimple was observed to develop after 13 s. This system is ultimately unstable in that the silicone oil film between the glycerol drops continues to thin and eventually the drops coalesced. The time scale of the approach towards coalescence is consistent with the tangentially immobile hydrodynamic boundary condition at the glycerol-silicone oil interface.

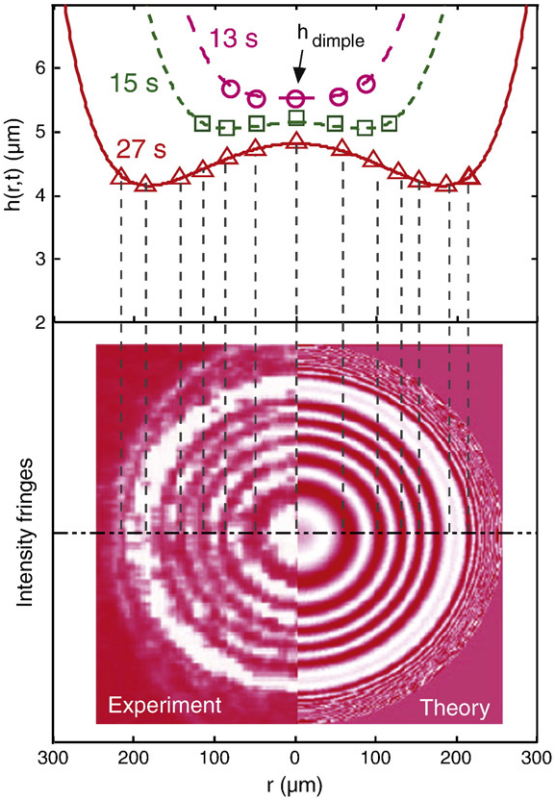

Fig. 5. The profile of the silicone oil film trapped between two glycerol drops that are driven together until 27 s. A dimple develops at 13 s at a separation of 5.5 μm. Note the very different horizontal and vertical scales. The symbols represent the experimental data that were obtained from the interference patterns such as the one shown below for 27 s. The solid lines represent the numerical solution. The right side of the interference pattern shows a numerical reconstruction based on the SRYL theory, the left hand side is the observed experimental pattern.

5.1.2. Bubble against quartz plate

The evolving shape of a water film trapped between an expanding bubble that has been pressed against an optically flat hydrophilic quartz plate has been measured by an optical method [76,95,96]. The bubble, initially 40 μm from the quartz plate, with unperturbed radius 1.16 mm, was expanded from an orifice with diameter 2 mm in a fraction of a second. The shape of the trapped water film that subsequently drained was recorded. The final equilibrium film was stabilized by electrical double layer repulsion between the quartz surface and the bubble, and depending on the added electrolyte concentration, the drainage process took up to 200 s.

In a drainage experiment, the film thickness at a fixed radial position r is measured as a function of time with a resolution of about 30 μm. The film profile $h(r,t)$ is then re-constructed from repeating such measurements at different positions [76,95,96], proving implicitly the reproducibility of the experiments.

A comparison of the experimental and predicted profiles of the non-equilibrium evolving water film is given in Fig. 6 [97]. Again the time scale of the drainage process is consistent with a tangentially immobile hydrodynamic boundary condition at the bubble surface and a no-slip boundary condition at the quartz plate.

5.1.3. Mercury drop against mica plate

The time evolution of the shape of the aqueous electrolyte film trapped between a mercury drop and an approaching or receding molecularly smooth mica plate has been measured by tracking interference fringes of equal chromatic order [98,99]. The surface potential of the conducting mercury drop was controlled independently to give repulsive or attractive electrical double layer disjoining pressures that allowed the evolution of stable and coalescing films to be investigated. We highlight the results of two experiments that demonstrate how an initially stable film responds to electrical and mechanical perturbations [87,100].

In Fig. 7, we show the collapse of an initially stable film formed between the mica plate and the mercury drop that are both negatively charged. The film was stabilized by electrical double layer repulsion. At $t = 0$, the sign of the potential of the mercury drop was changed to positive so the electrical double layer interaction became attractive and caused the film to collapse. For the most part, the collapse process retained axial symmetry and the mercury drop jumped into contact with the mica plate at the edge of the film where the electrolyte can easily drain from the film. However, it is entirely possible that the axial symmetry can be broken at the final moment of collapse, during a time that is too short to be resolved by the experiment.

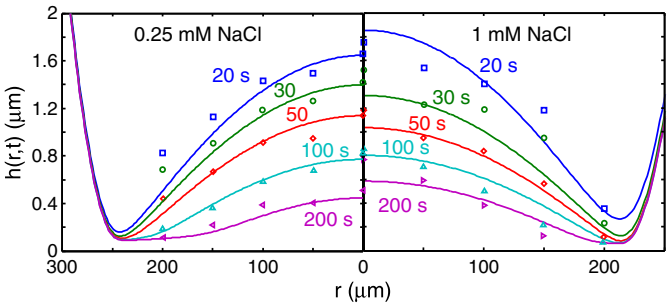

Fig. 6. The axisymmetric shape of the draining water film thickness, $h(r,t)$ as a function of position, r between a bubble and a quartz plate in 0.25 mM and 1 mM NaCl. Experiments (symbols), theory (solid lines).

Author's personal copy

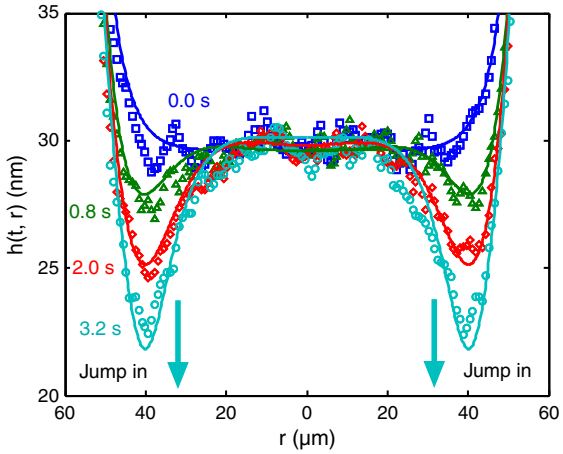

Fig. 7. An initial stable equilibrium aqueous electrolyte film (0.1 mM KCl) between a mica plate and a mercury drop with surface potential of the same sign as the mica is made to collapse by changing the polarity of the conducting mercury drop at $t=0$. The profile of the collapsing axisymmetric film is shown at $t=0$ s, 0.8 s, 2.0 s and finally at 3.2 s just before the mercury jumped into contact with the mica plate. Experiments (symbols), theory (solid lines).

What is clear is that the collapse process is predicted with qualitative accuracy by the SRYL model. There is no evidence of the mechanism of thermal fluctuations that has been postulated as being the key mechanism for initiating drop coalescence [101].

In another experiment, after the formation of an equilibrium water film between the mica plate and the mercury drop, stabilized by electrical double layer repulsion, the mica plate was retracted very rapidly from the mercury drop. The deformational response of the mercury drop to such a perturbation, prior to jumping apart, is shown in Fig. 8 together with predictions from the SRYL model.

Prior to the mica plate separating completely from the mercury drop, portions of the aqueous film actually became thinner during the transition period. This slightly counter-intuitive behavior arises because the deformable mercury interface is able to respond to the attractive hydrodynamic pressure generated in the film when the mica plate was retracted rapidly. For the result in Fig. 8, if the disjoining pressure is strongly attractive at below ~80 nm it is possible that the retraction of the mica plate can induce collapse of the aqueous film rather than being able to separate from the mercury drop. Such coalescence on separation behavior has now been observed directly using the atomic force microscope (see Section 5.2).

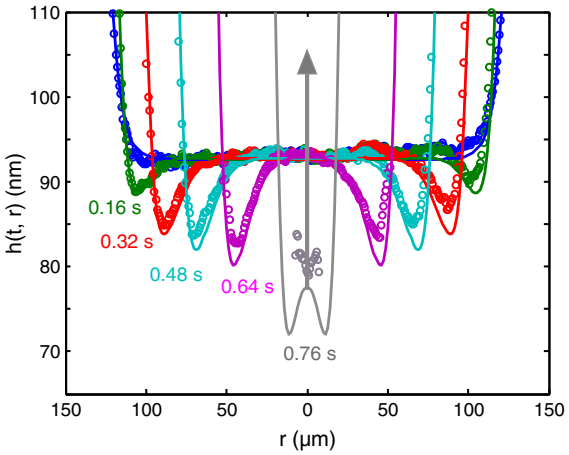

Fig. 8. The response of the equilibrium aqueous electrolyte film (0.1 mM KCl) between a mica plate and a mercury drop as the mica plate is retracted very rapidly from the drop. Before the mica and the mercury drop separate, parts of the aqueous film became thinner in transition. Experiments (symbols), theory (solid lines).

5.2. Dynamic force measurements

We highlight examples of non-equilibrium force measurements involving deformable drops [102–107] and bubbles [90,108,109] using the atomic force microscope (AFM). The observed features that arise from dynamic deformations are compared with quantitative predictions of the SRYL model.

5.2.1. Drop–sphere interaction

An example of the comparison between AFM experiment and theory for non-equilibrium forces between a silica micro-sphere and a tetradecane emulsion drop in water with 5 mM SDS is shown in Fig. 9 [102]. There is very good agreement between experiment and theory particularly in relation to the details of the hysteretic loop between the approach and retraction branch of the force-displacement curve in relation to different drive velocities. For these results, the predictions of the analytic force-formula, Eq. (4.4.1), are also in good quantitative agreement with experiments when the force becomes repulsive.

5.2.2. Drop–drop interaction

Examples of the non-equilibrium force as a function of time between two decane emulsion drops in 3 mM SDS and 1 mM $NaNO_3$ are shown in Fig. 10 [106]. For displaying results of dynamic force measurements it is preferable to show the explicit time dependence of the measured force because the cantilever displacement, for example in Fig. 9, does not contain direct information about time.

Again the SRYL model is capable of providing accurately the time dependence and variations of the depth of the retraction minimum with drive speed.

5.2.3. Bubble–bubble interaction

The simple experiment of driving two bubbles together or separating them in a well controlled and characterized manner while measuring directly the dynamic force between them has only been attempted with quantitative success recently using the atomic force microscope [90]. In the experiment, one bubble was mounted on the substrate and the other anchored at one end of a rectangular

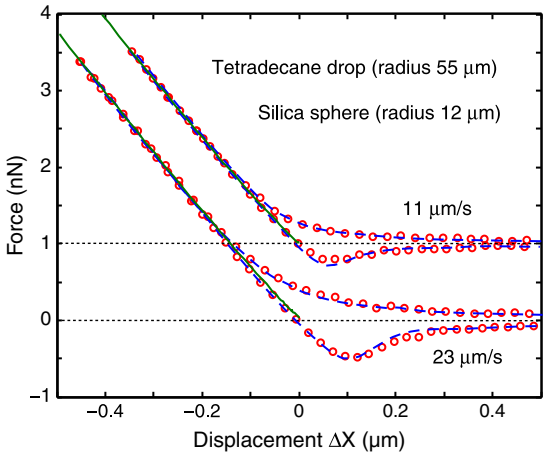

Fig. 9. The non-equilibrium force between a micro-sphere and a tetradecane drop in 5 mM SDS solution measured on the AFM as a function of cantilever displacement. For visual clarity, the zero force level for results at 11 μm/s has been displaced vertically by 1 nN. Theoretical results from the SRYL model: - - - and from Eq. (4.4.1): —, experiments (symbols).

Author's personal copy

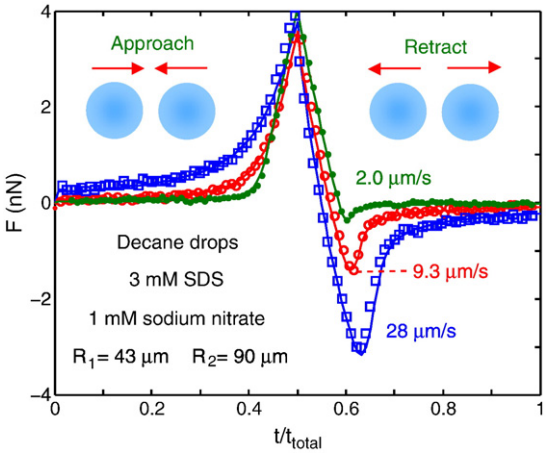

Fig. 10. The non-equilibrium force, measured on the AFM as a function of time for different drive velocities between two decane drops in an aqueous solution that contains 3 mM SDS and 1 mM $NaNO_3$ solution. The time axis is scaled by the total time of the collision, t_{total}. Results from the SRYL model: —, experiments (symbols).

force-sensing cantilever. The other end of the cantilever was driven towards the substrate at a nominal speed of ~50 μm/s.

Three different collision modes were employed in order to study bubble collision and coalescence phenomena:

(1) Approach only collision: In this case the cantilever is moved at constant speed while the repulsive force between the bubbles increased monotonically with time. For two bubbles with radii 62 μm and 86 μm and initial separation of 5.5 μm, the measured force is shown in Fig. 11a as a function of time. The bubbles coalesced when the force reached about 150 nN.

(2) Approach-Stop collision: Here, the cantilever was driven towards the substrate at the same nominal speed but was then stopped while the interaction between the bubbles evolved towards the final state. The force corresponding to such a collision between bubbles with radii 67 μm and 85 μm and initial separation of 1.65 μm, is also shown in Fig. 11a. Note that after the cantilever stopped, the bubbles continued to evolve under an almost constant force condition (~27 nN) before coalescence eventually occurred.

(3) Approach-Retract collision: In the third mode of collision the cantilever was driven towards the substrate at the same nominal speed for a predetermined time interval and then retracted at the same speed. The outcome of such a collision depended rather sensitively on the initial separation for the same maximum displacement of the cantilever. The key determinant is the distance over which the two bubbles have been pushed together beyond the point of contact if they did not deform. For a pair of bubbles with the same radii (74 μm) at an initial separation of 2.45 μm, the force (Fig. 11b) reached a maximum of about 8 nN and then decreased during the retraction phase, reached a minimum of about −6 nN in magnitude before separating eventually. No coalescence occurred for this case and the force curves are similar to those observed in drop–particle and drop–drop experiments.
The experiment was repeated with the same bubbles and the same cantilever displacement function, but starting at a smaller initial separation of only 2.05 μm. The force reached a larger maximum value around 18 nN (Fig. 11b). But instead of reaching a minimum during the retraction phase as in the previous Approach-Retract case, the bubbles coalesced instead during the separation stage. This counter intuitive behavior is similar to the results observed in Section 5.1.3 when the mica plate was retracted rapidly from a proximal mercury drop separated by a stable film.

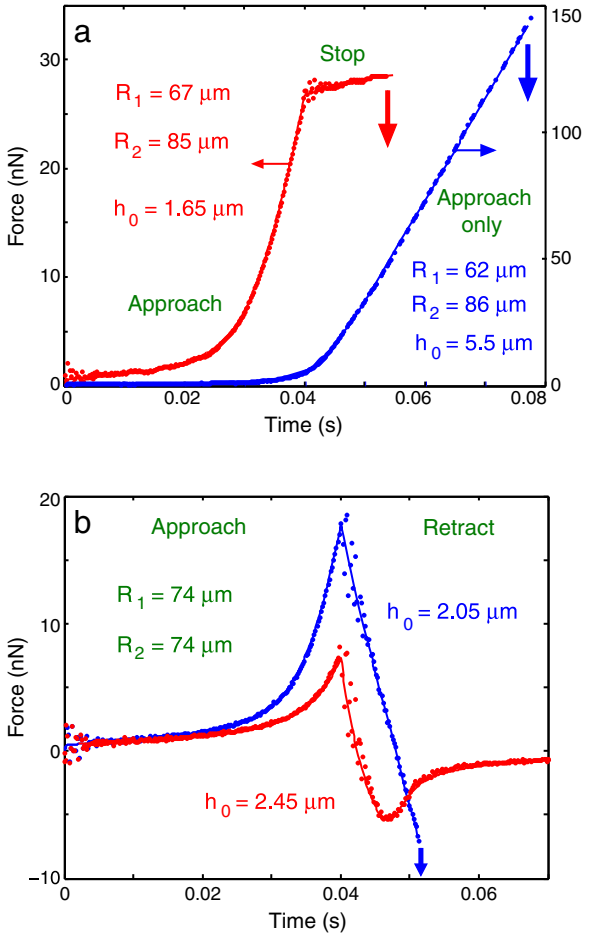

Fig. 11. The time-dependent force between two bubbles (radii 50–100 μm) during collision events at a nominal drive speed of ~50 μm/s in 0.5 M $NaNO_3$ aqueous electrolyte: experiments (symbols), theory (solid lines). Coalescence is indicated by down arrows. The results of three collision protocols are shown: (a) Approach only and Approach-Stop. The left vertical axis represents the "Approach Stop" force values (maximum ~27 nN), while the right vertical axis represents the 'Approach only' case (maximum ~150 nN). The origin of time is arbitrary. (b) Approach-Retract for the same bubble pair at different initial separation, h_o.

Detailed forms of the non-equilibrium force curves for different collision modes described above are predicted with quantitative accuracy by the SRYL model. Furthermore, the same theory also predicted correctly the coalescence time under all three different collision scenarios [90].

6. Conclusion

In this review we have given a detailed development of the Stokes–Reynolds–Young–Laplace (SRYL) equations that provided a consistent account of non-equilibrium interactions between deformable drops and bubbles which included surface forces, hydrodynamic effects and surface deformations in an internally consistent way. Phenomena relevant on the scale of the drop size such as how the drops are driven together are imposed as appropriate boundary conditions for the SRYL equations that focus on describing deformations on the scale of the thin film between interacting drops. The model is applicable in the parameter regime relevant to collision of drops in the 100 μm size range and relative approach velocities that span Brownian thermal velocities of such emulsion drops. It gives accurate predictions of the dynamic force measured using the atomic force microscope for controlled collusions involving deformable

Author's personal copy

bubbles and drops. The model is equally capable of predicting space and time deformations of draining films trapped by drops and bubbles.

By comparing with results from a variety of experiments on non-equilibrium deformations or forces, we found that the characteristic time-dependence of such experiments in aqueous systems is consistent with the tangentially immobile boundary conditions at the liquid–liquid and liquid–gas interfaces. In particular, bubble–bubble coalescence times in aqueous electrolyte are predicted with quantitative accuracy by the SRYL model. Since the shear rate in these experiments is low, with capillary number ~10^{-6}, it appears that trace amounts of surface-active materials at the interfaces, particularly at aqueous interfaces, would be sufficient to arrest interfacial flow and give rise to the tangentially immobile condition [108,109]. Although there are numerous studies of the Marangoni effect due to the presence of interfacial surface-active materials, the transition from the tangentially mobile boundary condition for clean interfaces to the tangentially immobile behavior due to surface-active species occurs over a relatively narrow range of surface concentration or the associated change in interfacial tension. Studies at the liquid–gas [110] and liquid–liquid [111] interfaces suggest that a surface concentration that lowers the interfacial tension by less than 1 mN/m, which is below the precision of many surface tension measurement techniques, is sufficient to render such interfaces immobile. This may be one reason why all the experimental results we considered appear to be consistent with the tangentially immobile condition. Furthermore, the deformability of the interfaces means that the local shear rates will not attain high values that might be expected to exist in the thin liquid layer between rigid surface that are being driven together. For interacting deformable drops and bubbles, when the sum of the hydrodynamic and disjoining pressure exceeds the Laplace pressure, the interfaces will flatten while maintaining an almost constant film thickness. This mechanism then allows the local shear rate to remain small even though the interaction force increases through increasing the effective interaction area through deformation. For systems driven at higher capillary numbers ($\geq 10^{-2}$), there is experimental evidence that both mobile and immobile interfacial conditions have been observed [112], but a quantitative theoretical explanation based on direct numerical simulations remains elusive. Such calculations are also computationally expensive and can take up to 500 CPU hours on a workstation to compute a single collision event [111].

For a long time, it has been accepted that coalescence required the development of thermally driven fluctuating surface waves as a triggering mechanism. Our comparisons with direct force measurements and responses of stable films to mechanical and electrical perturbations provided no evidence for the existence of this postulated mechanism. This is also supported by available direct numerical simulation results [111,112]

What is clear is that the modeling of non-equilibrium behavior involving deformable drops and bubbles must treat forces and deformations in a consistent way. Approaches based on the Reynolds Flat Film model that make assumptions about the geometry of interfacial deformations lack quantitative predictive capabilities.

Acknowledgments

Partial support provided to DYCC by the Australian Research Council through the Discovery Projects and Linkage Projects schemes is gratefully acknowledged. DYCC is an Adjunct Professor at the National University of Singapore and a Visiting Scientist at the Institute of High Performance Computing.

We thank one of the referees for extensive comments and suggestions that helped improve the manuscript significantly.

References

[1] Derjaguin BV, Landau L. Acta Physicochim URSS, 1941;14:663. Reprinted inProg Surf Sci 1993;43:30.
[2] Verwey EJW, Overbeek JThG. Theory of the stability of lyophobic colloids. Amsterdam: Elsevier; 1948.
[3] Derjaguin BV, Kussakov M. Acta Physicochim URSS, 1939;10:25. Reprinted inProg Surf Sci 1992;40:26.
[4] Scheludko A. Adv Colloid Interface Sci 1967;1:391.
[5] Chan DYC, Horn RG. J Chem Phys 1985;83:5311.
[6] Horn RG, Israelachvili JN. J Chem Phys 1981;75:1400.
[7] Israelachvili JN. J Colloid Interface Sci 1986;110:263.
[8] Klein J, Kumacheva E, Mahalu D, Perahia D, Fetters LJ. Nature 1994;370:634.
[9] Neto C, Evans DR, Bonaccurso E, Butt H-J, Craig VSJ. Rep Prog Phys 2005;68:2859.
[10] Lauga E, Brenner MP, Stone HA. Handbook of experimental fluid dynamics (Ch 19). In: Tropea C, Yarin A, Foss JF, editors. Springer; 2007.
[11] Honig CDF, Ducker WA. Phys Rev Lett 2007;98:028305.
[12] Honig CDF, Ducker WA. J Phys Chem C 2008;112:17324.
[13] Henry CL, Craig VSJ. Phys Chem Chem Phys 2009;11:9514.
[14] Ducker WA, Xu Z, Israelachvili JN. Langmuir 1994;10:3279.
[15] Butt H-J. J Colloid Interface Sci 1994;166:109.
[16] Aston DE, Berg JC. J Colloid Interface Sci 2001;235:162.
[17] Nespolo SA, Chan DYC, Grieser F, Hartley PG, Stevens GW. Langmuir 2003;19:2124.
[18] Derjaguin BV. Kolloid Z 1934;69:155.
[19] White LR. J Colloid Interface Sci 1983;95:286.
[20] Fogden A, White LR. J Colloid Interface Sci 1990;138:414.
[21] Stefan J. Sitzber Akad Wiss Wien. Math-Naturw Kl 1874;69:713.
[22] Reynolds O. Philos Trans R Soc London 1886;177:157.
[23] Yiantsios SG, Davis RH. J Fluid Mech 1990;217:547.
[24] Baldessari F, Leal LG. Phys Fluids 2006;18:013602.
[25] Yoon Y, Baldessari F, Ceniceros HC, Leal LG. Phys Fluids 2007;19:102102.
[26] Janssen PJA, Anderson PD, Peters GWM, Meijer HEH. J Fluid Mech 2008;567:65.
[27] Young T. Philos Trans R Soc London 1805;95:65.
[28] Laplace P-S. Mécanique célesteSupplement to the tenth edition. ; 1806.
[29] Gauss CF. Principia generalia theoriae figurae fluidorum in statu aequilibrii, Dieterichs; 1830.
[30] Lamb H. Hydrodynamics. Cambridge University Press; 1932.
[31] Yeh EK, Newman J, Radke CJ. Colloids Surf, A 1999;156:525.
[32] Chan DYC, Dagastine RR, White LR. J Colloid Interface Sci 2001;236:141.
[33] Starov VM, Velarde MG, Radke CJ. Wetting and spreading dynamics. CRC Press; 2007.
[34] Butt H-J, Kappl M. Surface and interfacial forces. Wiley-VCH; 2010.
[35] Chan DYC, Klaseboer E, Manica R. Soft Matter 2010, doi:10.1039/C0SM00812E.
[36] Beer A. Tractatus de theoria mathematica phaenomenorum in liquidis actioni gravitatis detractis observatorum. Bonn; 1857.
[37] Reinold AW, Rucker AW. Philos Trans R Soc London 1886;177:627.
[38] Valkovska DS, Danov KD, Ivanov IB. Colloids Surf, A 1999;156:547.
[39] Allan RS, Charles GE, Mason SG. J Colloid Sci 1961;16:150.
[40] Clasohm LY, Connor JN, Vinogradova OI, Horn RG. Langmuir 2005;21:8243.
[41] Ajaev VS, Tsekov R, Vinogradova OI. Phys Rev E 2008;78:031602.
[42] Platikanov D. J Phys Chem 1964;68:3619.
[43] Burrill KA, Woods DR. J Colloid Interface Sci 1969;30:511.
[44] Burrill KA, Woods DR. J Colloid Interface Sci 1973;42:15.
[45] Chesters AK, Hofman G. Appl Sci Res 1982;38:353.
[46] Hartland S, Yang B, Jeelani SAK. Chem Eng Sci 1994;49:1313.
[47] Danov KD, Gurkov TD, Dimitrova T, Ivanov IB, Smith D. J Colloid Interface Sci 1997;188:313.
[48] Klaseboer E, Chevaillier J-Ph, Gourdon C, Masbernat O. J Colloid Interface Sci 2000;229:274.
[49] Coons JE, Halley PJ, McGlashan SA, Tran-Cong T. Adv Colloid Interface Sci 2003;105:3.
[50] Chan DYC, Manor O, Connor JN, Horn RG. Soft Matter 2008;4:471.
[51] Bardos DC. Surf Sci 2002;517:157.
[52] Attard P, Miklavcic SJ. Langmuir 2001;17:8217.
[53] Batchelor GK. An introduction to fluid dynamics. Cambridge University Press; 1967.
[54] Leal LG. Advanced transport phenomena: fluid mechanics and convective transport. Cambridge University Press; 2007.
[55] Levich VG. Physicochemical hydrodynamics. Prentice Hall; 1962.
[56] Navier CLMH. Mem Acad Sci Inst Fr 1823;6:389.
[57] Vinogradova OI. Langmuir 1995;11:2213.
[58] Craig VSJ, Neto C, Williams DRM. Phys Rev Lett 2001;87:054504.
[59] Bonaccurso E, Kappl M, Butt H-J. Phys Rev Lett 2002;88:076103.
[60] Bonaccurso E, Butt H-J, Craig VSJ. Phys Rev Lett 2003;90:144501.
[61] Davis RH, Schonberg JA, Rallison JM. Phys Fluids A 1989;1:77.
[62] Abid S, Chesters AK. Int J Multiph Flow 1994;20:613.
[63] Edwards SA, Carnie SL, Manor O, Chan DYC. Langmuir 2009;25:3352.
[64] Yeo LY, Matar OK, de Ortiz ESP, Hewitt GF. J Colloid Interface Sci 2001;241:233.
[65] Yeo LY, Matar OK, de Ortiz ESP, Hewitt GF. J Colloid Interface Sci 2003;257:93.
[66] Yiantsios SG, Davis RH. J Colloid Interface Sci 1991;144:412.
[67] Okazaki S. Bull Chem Soc Jpn 1964;37:144.
[68] Duineveld PC. J Fluid Mech 1995;292:325.
[69] Wu M, Gharib M. Phys Fluids 2002;14:L49.
[70] Malysa K, Krasowska M, Krzan M. Adv Colloid Interface Sci 2005;114–115:205.
[71] Parkinson L, Sedev R, Fornasiero D, Ralston J. J Colloid Interface Sci 2008;322:168.

Author's personal copy

[72] Klaseboer E, Manica R, Chan DYC, Khoo BC. Eng Anal Boundary Elem 2011;35:489.
[73] Parkinson L, Ralston J. J Phys Chem C 2010;114:2273.
[74] Manica R, Parkinson L, Ralston J, Chan DYC. J Phys Chem C 2010;114:1942.
[75] Ivanov IB, Dimitrov DS, Somasundaran P, Jain RK. Chem Eng Sci 1985;40:137.
[76] Hewitt D, Fornasiero D, Ralston J, Fisher LR. J Chem Soc Faraday Trans 1993;89:817.
[77] Sanfeld A, Steinchen A. Adv Colloid Interface Sci 2008;140:1.
[78] Jeelani SAK, Hartland S. J Colloid Interface Sci 1993;156:467.
[79] Manev E, Tsekov R, Radoev B. J Dispersion Sci Technol 1997;18:769.
[80] Tsekov R. Colloids Surf, A 1998;141:161.
[81] Tsekov R, Evstatieva E. Progr Colloid Polym Sci 2004;126:93.
[82] Manev ED, Nguyen AV. Adv Colloid Interface Sci 2005;114–115:133.
[83] Chesters AK. Trans Inst Chem Eng A 1991;69:259.
[84] Manica R, Klaseboer E, Chan DYC. Soft Matter 2008;4:1613.
[85] Chan DYC, Klaseboer E, Manica R. Soft Matter 2009;5:2858.
[86] Leal LG. Phys Fluids 2004;16:1833.
[87] Manica R, Connor JN, Clasohm LY, Carnie SL, Horn RG, Chan DYC. Langmuir 2008;24:1382.
[88] Bremond N, Thiam AR, Bibette J. Phys Rev Lett 2008;100:024501.
[89] Gunes DZ, Clain X, Breton O, Mayor G, Burbidge AS. J Colloid Interface Sci 2010;343:79.
[90] Vakarelski IU, Manica R, Tang X, O'Shea SJ, Stevens GW, Grieser F, Dagastine RR, Chan DYC. PNAS 2010;107:11177.
[91] Lai A, Bremond N, Stone HA. J Fluid Mech 2009;632:97.
[92] Chan DYC, Klaseboer E, Manica R. Soft Matter 2010;6:1809.
[93] Manica R, Connor JN, Dagastine RR, Carnie SL, Horn RG, Chan DYC. Phys Fluids 2008;20:032101.
[94] Mahanty J, Ninham BW. Dispersion forces. Academic Press; 1976.
[95] Fisher LR, Mitchell EE, Hewitt D, Ralston J, Wolfe J. Colloids Surf 1991;52:163.
[96] Fisher LR, Hewitt D, Mitchell EE, Ralston J, Wolfe J. Adv Colloid Interface Sci 1992;39:397.
[97] Manica R, Chan DYC. Phys Chem Chem Phys 2011;13:1434.
[98] Connor JN, Horn RG. Langmuir 2001;17:7194.
[99] Connor JN, Horn RG. Faraday Discuss 2003;123:193.
[100] Manica R, Connor JN, Carnie SL, Horn RG, Chan DYC. Langmuir 2007;23:626.
[101] Ivanov IB. Thin liquid films: fundamentals and applications. New York: Marcel Dekker Inc; 1988.
[102] Webber GB, Manica R, Edwards SA, Carnie SL, Stevens GW, Grieser F, Dagastine RR, Chan DYC. J Phys Chem C 2008;112:567.
[103] Webber GB, Edwards SA, Stevens GW, Grieser F, Dagastine RR, Chan DYC. Soft Matter 2008;4:1270.
[104] Dagastine RR, Stevens GW, Chan DYC, Grieser F. J Colloid Interface Sci 2004;273:339.
[105] Dagastine RR, Chau TT, Chan DYC, Stevens GW, Grieser F. Faraday Discuss 2005;129:111.
[106] Dagastine RR, Manica R, Carnie SL, Chan DYC, Stevens GW, Grieser F. Science 2006;313:210.
[107] Dagastine RR, Webber GB, Manica R, Stevens GW, Grieser F, Chan DYC. Langmuir 2010;26:11921.
[108] Manor O, Vakarelski IU, Tang X, O'Shea SJ, Stevens GW, Grieser F, Dagastine RR, Chan DYC. Phys Rev Lett 2008;101:024501.
[109] Manor O, Vakarelski IU, Stevens GW, Grieser F, Dagastine RR, Chan DYC. Langmuir 2008;24:11533.
[110] Manor O, Chan DYC. Langmuir 2009;25:8899.
[111] Dai B, Leal LG. Phys Fluids 2008;20:040802.
[112] Yoon Y, Hsu A, Leal LG. Phys Fluids 2007;19:023102.
[113] Rodrigues TS, Butt H-J, Bonaccurso E. Coll Surf A 2010;354:72.